U. S. GEOLOGICAL SURVEY

SAUDI ARABIAN MISSION

TECHNICAL RECORD 10

(INTERAGENCY REPORT 349)

GEOPHYSICAL INVESTIGATIONS IN THE MAHD ADH DHAHAB DISTRICT, KINGDOM OF SAUDI ARABIA

by

Mark E. Gettings

with a section on

SHALLOW SEISMIC REFRACTION PROFILES

by

Habib Merghelani* and Mark E. Gettings

U. S. Geological Survey
Open-File Report 81-828

U.S. Geological Survey
Jiddah, Saudi Arabia

1981

*Saudi Arabia Directorate General of Mineral Resources

The work on which this report was based was performed in accordance with a cooperative agreement between the U.S. Geological Survey and the Ministry of Petroleum and Mineral Resources.

The quadrangle identification method used in U.S. Geological Survey Saudi Arabian Mission reports is shown below.

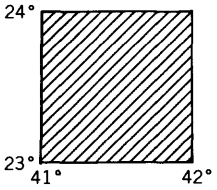

23/41

1-degree quadrangle

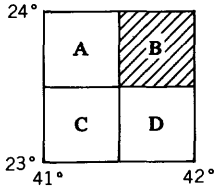

23/41 B

30-minute quadrangle

CONTENTS

ILLUSTRATIONS

[Plates are in back pocket]

Page

TABLES

Page

GEOPHYSICAL INVESTIGATIONS IN THE MAHD ADH DHAHAB DISTRICT, KINGDOM OF SAUDI ARABIA

by

Mark E. Gettings

ABSTRACT

Extensive geophysical investigations have been carried out at the Mahd adh Dhahab gold mine, Kingdom of Saudi Arabia, by the U.S. Geological Survey Saudi Arabian Mission as part of a multidisciplinary study of the district. The three major objectives of the study were: 1) to define unexposed areas of probable sulfide mineralization for further exploration; 2) to infer the geologic relations beneath the covered areas surrounding Jabal Mahd adh Dhahab; and 3) to provide further constraints on structural and genetic models of the geologic history. The study area measures 1.5 km in a north-south direction by 2.9 km in an east-west direction and is centered approximately on the mine workings. Work was completed during the period between mid-1973 and September 1975 by geophysicists from the Directorate General of Mineral Resources and the U. S. Geological Survey, and additional data were acquired by contract with the Arabian Geophysical and Surveying Company.

The geophysical data base for the study includes induced polarization and apparent-resistivity surveys (mise a la masse) method) for six electrode configurations, a self-potential survey, a TURAM electromagnetic survey, a total-magnetic field survey, a gamma-ray spectrometer survey, four shallow seismic refraction profiles, self-potential and single-point resistivity logs of three drill holes, and laboratory studies of the magnetic, electrical-resistivity, and chargeability properties of selected rock specimens.

Several areas of anomalous magnetic and electrical response were discovered during the survey work. The maximum induced polarization effect observed was 110 mV/V, the largest negative self-potential anomaly was about -100 mV, and several areas of apparent resistivity less than 100 ohms-m were delineated. In general, however, responses to the electrical methods were not large.

A qualitative analysis of the data defined five target areas, none of which has been tested adequately to date. Analysis of the seismic refraction, residual-gravity anomaly and magnetic-field data sets resulted in the definition of a minimum fault and fracture pattern in the covered area south of the mine and east of Jabal Mahd adh Dhahab. The distribution and trends of the inferred faults agree well with those exposed on bedrock, and zones of inferred mineralization correlate with the north- and

northeast-trending faults, but not with the northwest-trending ones. An eastern boundary of mineralization at depths less than 100-200 m is apparent in the data, and although targets east of the eastern boundary of the induced polarization survey area are not precluded, they seem unlikely. The geophysical data are consistent with a fault and fracture pattern associated with the folding of the rocks of the district into a northeast-plunging antiform, and subsequent mineralization controlled by these faults and fractures where they intersect favorable horizons for metasomatism.

From studies of the electric well logs, it appears that the logs of the northern and southern agglomeratic units can be correlated, suggesting that the agglomeratic part of the volcanic pile is structurally repeated along a north-south profile, rather than being two separate lithostratigraphic units. Analysis of magnetic anomalies on exposed andesite fault blocks and laboratory studies of the magnetic properties of the rocks of the district imply that the most probable sources of the magnetic anomalies mapped in the covered areas are buried fault blocks of andesite. Intrusives are not precluded, but the shallow depth estimates from the magnetic anomalies and the results of drilling place severe constraints upon their geometry. Laboratory measurements of the apparent resistivity and chargeability of selected samples of core from several drill holes show a wide range of variation, but a general relation of direct proportionality between chargeability and apparent resistivity is observed. This result is not surprising in light of the highly silicic nature of the host rocks and the association of sulfide mineralization with quartz veining in the district.

INTRODUCTION

Location and description

The Mahd adh Dhahab district, Kingdom of Saudi Arabia, is an area of extensive ancient and modern gold mining. The area is located (fig. 1) approximately 170 km southeast of Medina and 250 km north of Taif at lat 23°30'N. and long 40°53'E. The district, approximately 2 km^2, is immediately south of the village of Mahd adh Dhahab. Numerous ancient workings are present on the bedrock exposures of Jabal Mahd adh Dhahab, as well as open pits and extensive underground shafts and stopes made by the Saudi Arabian Mining Syndicate (SAMS) from 1939 to 1954. Most mining activity has been at Mine Hill, which forms the northeastern corner of the jabal. The abandoned SAMS cyanide-flotation plant and tailings pond cover an area of about 0.16 km^2 on the alluvial plain adjacent to the northeastern corner of Jabal Mahd adh Dhahab.

The deposit is located in a volcanic pile of andesitic to rhyolitic tuffs and agglomerates. Gold and silver metallization occurs in association with base metal sulfides where quartz veins intersect favorable horizons in the volcanic pile.

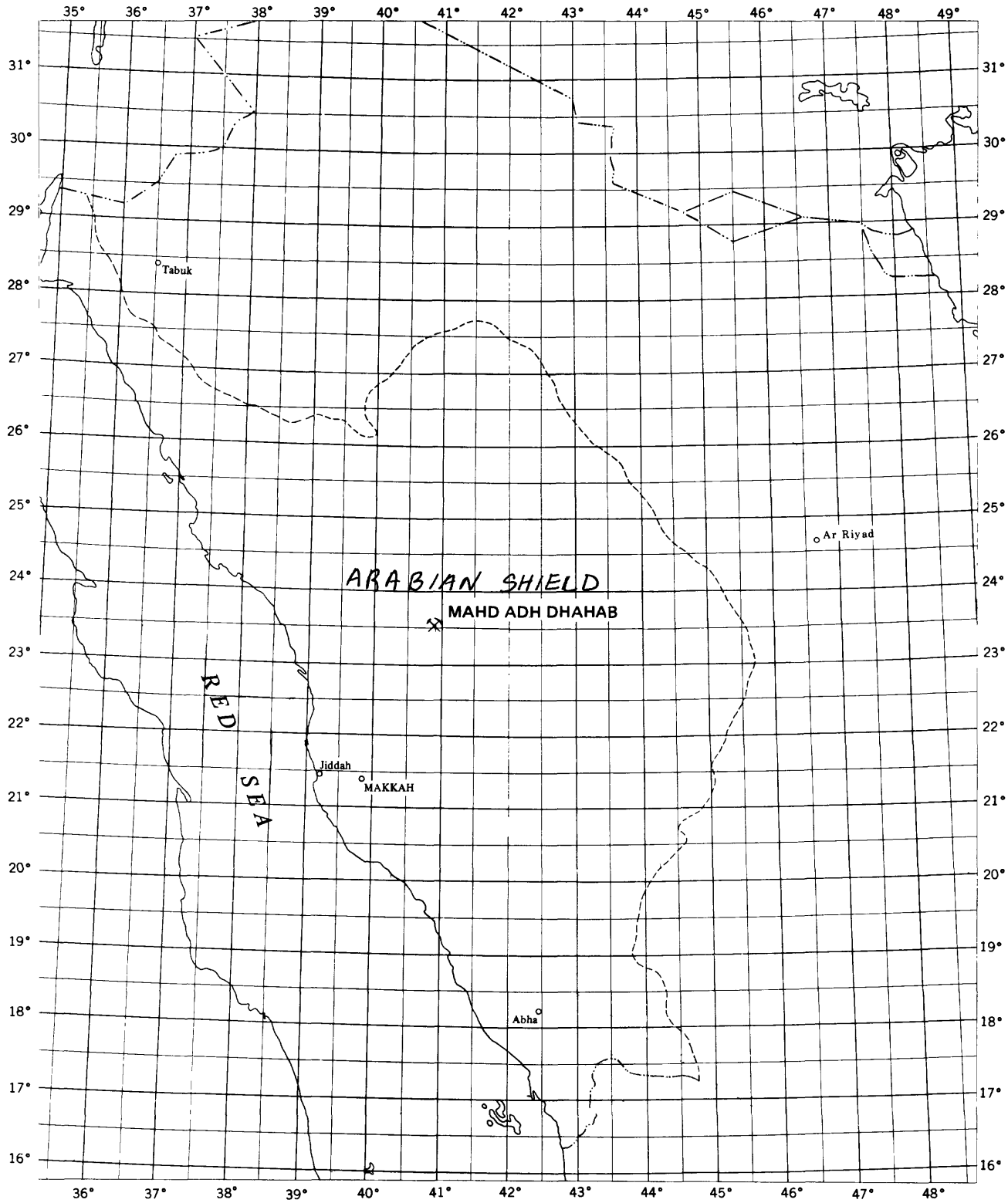

Figure 1.–Index map showing the location of the Mahd adh Dhahab gold mine, Kingdom of Saudi Arabia.

History of exploration

Mineral exploration of the Mahd adh Dhahab district has been carried out at irregular intervals from 1931 through the present. The chronology of geologic exploration of the area is well summarized by Worl (1978b). Previous geophysical exploration was limited to an airborne magnetometer-scintillation counter survey of the Aqiq area, which includes the Mahd adh Dhahab district, flown and compiled in 1962 for the Directorate General of Mineral Resources by Hunting Surveys Limited, (unpub. data) and several horizontal coil electromagnetic traverses on the western side of Jabal Mahd adh Dhahab (Davis and others, 1972). The electromagnetic survey, aside from estimates of a 60-m thick zone of weathering and(or) alteration, was somewhat inconclusive.

The United States Geological Survey (USGS), as a part of its work agreement with the Ministry of Petroleum and Mineral Resources, Kingdom of Saudi Arabia, has carried out an extensive investigation of the district since 1972. This study included geological mapping at a scale of 1:2500 (Luce and others, 1976), geochemical investigations (Roberts and others, 1978), placer gold deposit studies (Bagdady and others, 1978), a diamond drilling program and detailed geological mapping at a scale of 1:1000 (Worl, 1978b), and geophysical surveys of the area (this report). These combined studies culminated in the discovery of new mineralized zones with potential tonnage of gold and silver about equal to the total previously mined from the district and the delineation, by combined geological and geophysical means, of several promising target zones for further exploration.

In this report,

In addition to a presentation of the results with interpretation, the geophysical data are sufficiently documented so that they may be used by later investigators. This documentation makes the report more detailed, but is warranted because of active exploration in the district. Most data are in the form of contour maps only because the large amount of numerical data generated by this study prohibits its inclusion in a single report. All numerical data are available in the archives of the U.S. Geological Survey Saudi Arabian Mission, Geophysics Group, Jiddah, Saudi Arabia.

Acknowledgements

This work was carried out in accordance with the work agreement between the U.S. Geological Survey and the Ministry of Petroleum and Mineral Resources of the Kingdom of Saudi Arabia. Grateful acknowledgement is made to the Ministry of Petroleum and

Mineral Resources and the Directorate General of Mineral Resources (DGMR) for the support that made this study possible.

Habib Merghelani, Hisham Gazzaz, and Khalid Alageel, all from the DGMR, and Abdeen Uthman, USGS, aided in survey work and data reduction and interpretation. Mabruk Basahel, DGMR, aided in map compilation and preparation and Joseph Adams assisted in the ground magnetic survey. Maher Bazzari, USGS, assisted in the laboratory work. H. R. Blank, V. J. Flanigan, T. H. Kiilsgaard, R. J. Roberts, D. B. Stoeser, and R. G. Worl all contributed guidance, discussion, and suggestions to various stages of the project. B. M. North and L. D. North both contributed much time and effort to the reduction of the induced polarization (IP) data by digital computer methods.

GEOLOGICAL AND GEOCHEMICAL SETTING

Lithologies

The geologic relationships have been described in detail by several authors. A geologic summary is included here for convenience in discussions of the geophysical results and is drawn for the most part from Worl (1978a, b) and Luce and others (1976), all of which should be consulted in conjunction with this report.

The study area is composed of a series of Precambrian volcanic pyroclastic and clastic rocks of andesitic to rhyolitic composition deposited on a large diorite to granodiorite body. Tuffs, transported pyroclastic rocks, and clastic rocks predominate in the area, except in the southwestern corner, which is underlain mainly by andesitic flow rocks.

The clastic rocks contain fragments of andesitic to rhyodacitic volcanic rocks, silicic tuff, chert, feldspar grains, diorite, and pumice. The common minerals are chlorite, plagioclase, potassium feldspar, quartz, epidote, and minor amphibole. Lapilli and bombs of various sizes indicate that the rocks are a near-vent volcanic facies, at least in part.

The lithologic sequence of Luce and others (1976) will be followed in this report. In order of decreasing age it is the lower agglomerate, lower tuff, upper agglomerate, and upper tuff.

The lower agglomerate has been divided into lower, middle, and upper units and the upper agglomerate into a crystal-lithic tuff to agglomerate (lower unit) and a gray agglomerate (upper unit) by Worl (1978a, b). The stratigraphy is summarized in table 1, modified from Worl (1978a).

Table 1.--*Stratigraphy of the Mahd adh Dhahab mine area*

uta	AGGLOMERATE-CONGLOMERATE--Red to pale-green, characterized by abundance of pale-green dacite fragments; white, gray, and red tuff; red chert; fragmental plagioclase; locally abundant fragmental quartz. Coarse layering. Intercalated waterlain tuff and argillite
utt	ARGILLITE-CALCAREOUS TUFF--Fine-bedded gray argillite intercalated with calcareous and talcose, brown, massive to fine-bedded tuff and minor volcanic wacke. Local zones of massive talc
	----------Unconformity or fault----------
uaa	GRAY AGGLOMERATE--Subrounded fragments of white, red, and gray chert, siliceous tuff, pyrite-rich tuff, andesite to rhyodacite volcanic rock, and chlorite- and epidote-rich clots set in a gray, siliceous and pyritiferous groundmass. Local pink potassium feldspar scattered randomly through groundmass and fragments
	----------Local unconformity----------
uat	CRYSTALLITHIC TUFF TO AGGLOMERATE--Pale- to dark-green, with gray chert, brown to gray tuff, wispy chlorite, gray siliceous lapilli, locally abundant fragmental plagioclase, and andesite to rhyodacite volcanic rock set in gray, siliceous groundmass. Generally bedded and locally graded. Intercalated fine-grained massive green tuff. Pink potassium feldspar is locally abundant as a partial to total replacement of the fragmental plagioclase and to a lesser extent as scattered crystals through groundmass and all fragments
lt	TUFF AND SEDIMENTARY ROCKS--Fine-grained massive to finely bedded tuff, lapilli tuff, volcanic wacke, and sandstone. Highly potassium-feldspathized in the vicinity of the SAMS mine
lau	UPPER UNIT--Mafic agglomerate, mostly andesitic and chloritic fragments set in gray, siliceous groundmass, and mafic lapilli tuff, plagioclase crystal tuff, and massive cherty tuff. Local fragments of massive sulfide (?) and pyrite-rich tuff
lam	MIDDLE UNIT--Mafic agglomerate; agglomerate with andesite; chloritic, red, gray, and black massive tuff; and dioritic fragments in chlorite and epidote groundmass. Intercalated dense massive green to brown chert
lal	LOWER UNIT--Massive to slightly bedded andesite tuff and lapilli tuff with minor intercalated mafic agglomerate
	----------Unconformity----------
an	ANDESITE--Mostly dense to fine-grained; some crystalline units may be dioritic sills; few intercalated pyroclastic layers. Generally propylitically altered; in fault contact with lower agglomerate

Structure

Regional structural features are mainly northeast-trending faults and broad northeast-plunging folds; the Mahd adh Dhahab district is located in the nose of an antiform plunging northeast approximately 50°. Northwest-trending faults, probably associated with the Najd fault zone, are also present. A major right-lateral fault system trending northeast cuts the area beneath wadi fill in the southeastern part of the district (Goldsmith and Kouther, 1971).

The most obvious structural feature within the district itself is a north- to northeast-trending system of faults, shear zones, and extensive quartz veins. Several episodes of faulting and quartz vein and andesite dike emplacement have been recogized (Luce and others, 1976), and low-angle faults occur in the northern part of the area where the upper tuff is strongly folded (Worl, 1978b).

Rocks of the sequence are commonly well bedded, retain original textures and, in general, seem to be only slightly metamorphosed in a regional sense, if at all. Large areas of brecciation are present; some are associated with faulting but many are the result of folding of incompetent rock units. The geological features of the area are shown on plate 1, which has been compiled principally from the maps of Luce and others (1976) and Worl (1978a, b).

Structural analysis of all available attitude data enabled Worl (1978b) to subdivide the area into several structurally homogeneous blocks, each with its own axis and style of folding. These blocks are displayed on plate 2. The largest block, comprising the unmineralized central part of the district, is a north-dipping homocline; the other blocks define folding of the open flexural type. Flow and shear folds found in many higher grade metamorphic terranes are not observed here (Worl, 1978b). No evidence has been recognized for multiple episodes of folding, and the quartz veins are not folded. The veins in all cases seem to occupy preexisting faults or fractures, which were probably formed at the time of folding; some of the faults and shear zones are curvilinear in outcrop pattern (Worl, 1978b).

Mineralization

In the report area, gold, silver, copper, zinc, and lead metallization is always in association with quartz veins; however, not all quartz veins are metallized. The veins occur throughout the district but veining is most intense in an approximately north-trending zone through the mine area. Quartz veins occur as both massive and quartz-healed breccia types and range from a few millimeters to five meters in thickness. At least four episodes of veining can be recognized (Luce and others, 1976) with varying degrees of metallization.

The quartz veins contain subordinate bands of sulfides and chlorite and locally abundant potassium feldspar. The most intense metallization is in zones with a high density of quartz veins and stockworks and is found both in the veins and the altered wall rocks. The sulfides present are pyrite, chalcopyrite, sphalerite, galena, tetrahedrite, and argentite. Gold and silver occur as disseminated metals and as tellurides accompanying the sulfides.

Diamond core drilling, amounting to a total of 3720 m in 10 holes, tested several geological and geochemical targets. One hole, MD 10, tested an electromagnetic (EM) anomaly. The core logs of these holes, augmented by core logs from holes drilled by SAMS and also by the results of surface geochemical sampling, enabled two distinct ore zones to be outlined (Worl, 1978b). The first is that mined by the ancients and the SAMS operation, at the intersection of the upper agglomerate and zones of intense quartz veining. The second is at the intersection of the same zone of quartz veins and the upper unit of the lower agglomerate. In both cases, metallization is highest near the capping tuff unit and decreases with increasing distance downward from the tuff. Exploration targets therefore are those zones directly below the contact of the upper agglomerate and the upper tuff and those below the contact of the lower agglomerate and the lower tuff, in areas of intense quartz veining.

A surface geochemical chip-sampling program delineated several blocks of anomalous copper, lead, zinc, gold, and silver concentrations (Roberts and others, 1978). Values of copper and zinc are high enough in some blocks to be base metal ore (Roberts and others, 1978). Contours of average copper and gold values are shown on plate 2; the correlation between high copper and high gold values is noteworthy. However, this correlation does not always hold in detail; SAMS data and USGS drill core data show that zones of high base metal content contain gold, but not all areas of high gold content contain base metals.

The source of mineralization in the favorable horizons of the agglomerate was evidently hydrothermal solutions, rather than concentration of metals already existing in the mineralized horizons (Worl, 1978b). It seems, therefore, that the ore-forming fluids were brought in by the quartz-veining event.

The principal conclusions of the geological and geochemical studies are: 1) the principal structure of the layered rocks is a north-dipping homocline that is flexurally folded and extensively faulted; and 2) the ore-controlling factors are the intersection of intensely quartz-veined zones and the agglomerates where they are capped by rather impermeable tuff. The geophysical program was undertaken with the aims of completing the three-dimensional geological picture to a depth of about 200 m and exploring the areas of cover to the north and east of the outcrop exposure. In terms of exploration, the strategy was that,

inasmuch as gold and silver are generally associated with sulfide metallization, knowledge of sulfide distribution gained from geophysical exploration would provide possible gold and silver targets.

THE GEOPHYSICAL DATA

Base map and horizontal and vertical control

All ground geophysical survey work was carried out using a 1:2500-scale topographic map of the area as a base. This map was prepared by KLM* (originally Aerocarto N.V.) for a larger area at a smaller scale and later adapted and extended by USGS. A 50 m-square horizontal grid oriented north-south and east-west was surveyed in the area by USGS personnel in 1974 and 1975. The grid and base map are shown in plate 2; the areas covered by the various geophysical surveys are shown in figure 2. The USGS grid, marked by stone cairns, extends from 1000 m east to 1000 m west and from 600 m north to 800 m south. During the summer of 1975, the grid was extended by the Arabian Geophysical and Surveying Company (ARGAS) to 1500 m east. The grid origin is located approximately at long 40°51'49.47"E. and lat 23°30'03.21"N. In the following discussion, grid locations will be given as ordered pairs with the number of meters north or south of the origin as the first number, and the number of meters east or west of the origin as the second. For example, a point 670 m south and 430 m west of the origin would be referred to as "670S, 430W".

Induced polarization and apparent-resistivity measurements

Survey results

Survey description.--An induced polarization survey was carried out for USGS by ARGAS under an extension of a contract agreement between DGMR and ARGAS during the period 26 June 1975 to 10 September 1975. The current electrodes were set out for the mise a la masse method, whereby one electrode is in a conductive zone in a drill hole and the other is remote from the survey area. In this case, brass-rod electrodes, 50 cm by 3.5 cm in diameter, were put down drill holes MD 8, MD 9, and MD 10 at depths selected on the basis of both the geologic logs and the combined resistivity and self-potential logs run on the holes (the electric logs are discussed in a separate section below). Two remote electrodes were emplaced in pits on the surface approximately 3 km to the east and south respectively of the grid origin. The coordinates of all electrodes are given in table 2. With this array of electrodes, a total of six maps of the area from 500 m west to 500 m east and 800 m south to 600 m north were produced by reading the receiver at 50 m intervals at grid points along the east-west grid lines. For the area from 0 to 800 m south and from 0 to 500 m east, the current source was a Scintrex

*KLM Dutch Airlines

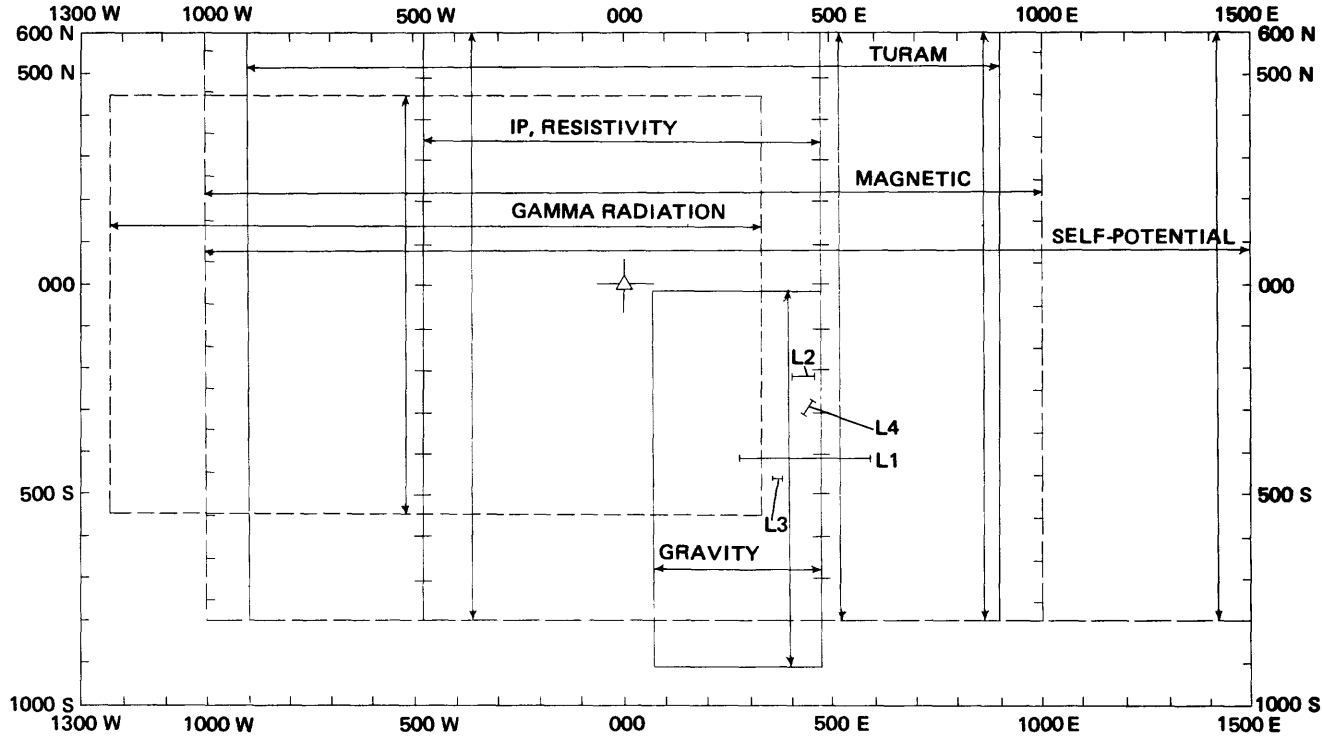

Figure 2.–Index map of geophysical surveys of the Mahd adh Dhahab district presented in this report. Coordinates are relative to the USGS 50-m grid described in this report. Lines L1 through L4 are shallow seismic refraction lines.

Table 2.--*Coordinates of the source electrodes used for the induced polarization and apparent-resistivity mise a la masse surveys*
[Coordinates and elevations are in meters]

Source	North-south coordinate	East-west coordinate	Elevation
MD 8	276S	028W	992.50
MD 9	421N	182W	886.25
MD 10	002S	294E	965.30
East ground	025S	3500E	1050 (estimated)
South ground	3700S	225E	1050 (estimated)

IPC 7 time-domain transmitter with 2.5 kW of power used at a 2 second pulse rate. The receiver used was a Scintrex IPR-8 set to integrate the signal from 130 milliseconds to 1690 milliseconds after the end of the transmitted pulse. Eight cycles were averaged for each reading, and commonly three readings were taken for each source-electrode pair of one remote and one downhole electrode. Although not stated in ARGAS field notes, porous pots and saturated copper sulfate solution are believed to have been used for the receiver electrodes, which were placed at the bases of the cairns making the grid. With this configuration, complete readings were taken at about thirteen 50-m dipole spreads per day.

Shortly after completion of this portion of the survey, a mechanical failure occurred in the transmitter. The necessary spare parts were not available, and for the rest of the survey area (50 m south to 600 m north, 0 to 500 m east, and 800 m south to 600 m north, 0 to 500 m west) MacPhar frequency-domain equipment was used. ARGAS field notes do not record the model of equipment used nor any other details except that the transmitter power was on the order of one kilowatt. In all, 42 days of field work were required to complete a total of 3404 induced polarization measurements.

The results were delivered to USGS in the form of the original field data sheets and contour maps of induced polarization (IP) effect, together with a short textual description of the survey and preliminary interpretation (ARGAS, 1975). The field data sheets were then coded and keypunched onto computer cards by USGS personnel and reduced by a computer program written for the purpose. Results of these calculations, which produced not only the IP effect but also apparent-resistivity and metallic-conduction factor values, were carefully checked against original field data sheets obtained from ARGAS. After correction of all errors detected, contour maps of the data were drawn by a computer-driven plotter. The resulting IP-effect (mV/V for time domain and percent-frequency effect for frequency domain) maps are presented in plates 3-8, the apparent-resistivity maps in plates 9-14, and the metallic-conduction factor maps in plates 15-20.

In these maps, all data that gave a consistent set of field readings, and for which there were no indication of problems in the field data, have been preserved, even if they result in "single-point" anomalies. The IP-field data are probably about 90 percent reliable because at least three readings were taken for each measurement and the receiver is unlikely to have been read incorrectly in the same way three times. In most cases, because of the lack of annotated field notes, it is impossible to form an objective basis for acceptance or rejection of an apparently good but highly anomalous set of readings. Most "single-point" anomalies therefore should be regarded as questionable. However,

in the zone of overlap of the frequency-domain and time-domain data (0 to 50S, 0 to 500E), several "single-point" anomalies are present in both data sets, and thus appear to be real. In many cases, particularly in the northwestern quadrant of the map, the anomalous zones are narrow bands striking northwest and northeast, so that in any east-west line they appear as "single-point" anomalies but have continuity across lines and must be regarded as real.

It is somewhat convenient to refer to the IP-effect, apparent-resistivity, and metal-factor maps by their current electrode configuration; thus the three maps whose current electrodes were in drill hole MD 8 and the east remote location are labeled "E08", while the maps for electrodes MD 8 and the south location are labeled "S08". This notation is used in the ensuing discussion of the general features of the maps.

General features of the IP-effect maps.--The IP-effect anomalies were considered notable if they exceeded three percent frequency effect in the frequency domain or 30 millivolts per volt in the time domain. In IP surveys of the mise a la masse type, negative as well as positive IP effects are commonly observed, particularly in environments that have high resistivity contrasts (Sumner, 1976). Because of the extensive quartz veining and areas of silicification in the Mahd adh Dhahab district, high resistivities are to be expected and, wherever conductors are present, large resistivity contrasts will be encountered. It should be noted further that negative IP effects are generally spatially associated with the positive, and that the anomaly may move laterally and certainly will change in intensity and perhaps even in polarity with different current electrode configurations (Sumner, 1976).

The major features of the IP-effect maps (pl. 3-8) are tabulated in table 3. First, the major trends in all the maps are northeast (azimuth approximately 035°) and northwest (azimuth approximately 140°); these trends imply that a fault and(or) fracture system controlled the deposition of sulfides. Second, a major conductive and at least partly mineralized fault and(or) shear zone divides the area along a trend of 035° from about 150S, 200E to 100N, 400E. This zone extends southwestward to about 600S, 100W, but acts in this area as an insulator. Because of the electrode configuration, this zone effectively isolates the area to the southeast from exploration by electrodes in MD 8 and MD 9. The area northwest of the zone is isolated when the electrode in MD 10 is used because the remote electrodes are in the southeastern block. Electrically, the zone acts as a sink in the northeastern part and as an insulator in the southwestern part when MD 8 or MD 9 electrodes are used, and as a sheet source when MD 10 is used. Third, the major sulfide target areas, in order of priority, appear to be: 1) 450S-750S, 0-200E; 2) 150S-100N, 200E-450E; 3) 450N-600N, 100W-400W; and 4) 450N-600N, 150E-400E. The areas 425S-650S, 50-150W and 200S-400S, 100E-175E are possible targets.

Table 3.--*General features of induced polarization-effect maps*

Map	Location of significant anomalies	Trends (azimuth)	Remarks
E08 (pl. 3)	a. 500S-600S, 150W-50E b. 350N-600N, 500W-100W c. 450N-600N, 100E-250E	035°, 140°	1. Anomalies a and b are larger ; c is least 2. Anomalies b and c have well developed bipolar character 3. SE quadrant of map is relatively featureless beyond a linear zone from 500S, 50E to 0, 300E 4. Zone of remark 3 truncates ridge of IP highs extending from NW corner of map to 150S, 100E
E09 (pl. 4)	a. 50N-50S, 250E-400E b. 450S, 150E c. 400N, 200W	035°, 140°; minor trend of 000°	1. Anomalous area c has complex bipolar character 2. Zone of remark 3, map E08 present, map features terminate against it from the NW, and area to SE of zone is relatively featureless 3. NE part of zone of remark 2 is evidently a conductor, probably a fault or shear zone, which is acting as a sink for current from MD 8 or MD 9, thus isolating area to SE from exploration using MD 8 or MD 9 as source electrodes

Table 3.--*General features of induced polarization-effect maps* [continued]

Map	Location of significant anomalies	Trends (azimuth)	Remarks
E10 (pl. 5)	a. 450S-750S, 0-250E b. 0-200S, 250-300E c. 200N, 225W d. 500N, 425E	035°, 140°; 090° in SW quadrant	1. Anomalous area a constitutes best exploration in the area 2. Anomalous area b shows well developed bipolar characteristics, extends in narrow zone N-S 3. Relief and structure in map are concentrated in SW quadrant SW of fault/shear zone. Electrode in MD 10 makes zone act as sheet source; remote electrode to east minimizes response NW of zone, but details structure to SW very well
S08 (pl. 6)	a. 550S, 50W b. 50N-100N, 100E c. 350N, 100W d. 500N, 150E-350E	035°, 140°; minor 090° in west half of map	1. Anomaly a is a target 2. Fault/shear zone acts as a sink, minimizing response on SW side 3. No anomaly at source electrode MD 8
S09 (pl. 7)	a. 500S, 25E to 50S,275E b. 650S-750S, 50W-200W c. 400S-550S, 425W d. 350N,175W & 500N,200W e. 100S, 0 to 100N, 125E f. 750S, 325E (small)	035°, 140°; minor 000°, 090° in NW quadrant of map	1. Negative anomalies at each end of high ridge a are possible bipolar effects 2. Anomalies of d associated with current electrode in MD 9 3. Internal structure of anomaly a suggests structures trending 140° are also mineralized 4. Response of anomaly e is weak 5. Isolating nature of fault zone a suppresses response in area to SE of zone

Table 3.--*General features of induced polarization-effect maps* [continued]

Map	Location of significant anomalies	Trends (azimuth)	Remarks
S10 (pl. 8)	a. 50S-100N, 275E b. 400S, 275E c. 550S, 75E d. 750S, 175E to 650S, 350E e. 450N, 475E (?) (weak)	035°, 140° 090°, 000° in west half of map	1. Fault zone behaves as a source, but does not respond anomalously as in S09 2. Anomaly a bipolar, associated with electrode anomaly b bipolar 3. Anomaly c is the main target anomaly 4. Anomaly e suggested only 5. Response in area NW of fault zone is suppressed by conductivity of fault zone and location of remote electrode to S in SE block

General features of the apparent-resistivity maps.--Because the apparent-resistivity values range over five orders of magnitude, common logarithms have been contoured in plates 9-14 rather than the values themselves. Areas having apparent resistivities of 100 ohms-m or less (contour value 2.0 or less on the plates) are regarded as being of interest.

The resistivity lows are generally elongated or at least oriented along linear zones and generally appear to be due to conducting fault or shear zones. A major feature of the apparent-resistivity maps, shown best on plates 11 and 12, is a northwest-trending conducting zone from 650S, 350E to 400N, 400W that truncates the northeast-trending zone discussed in the section on the IP-effect maps. The intersection (in the area of 250S, 150E) of this structure with the northeast-trending zone discussed above occurs where the zone changes character from a conductor in the northeast to an insulator in the southwest. Other major conductive areas on the maps are from 150S, 175E to 100N, 400E and 450N-600N, 300E-500E. A north-south band of low resistivity anomalies occurs in the area 750S-25S, 0-150W, but the anomalies within the band have northwest and northeast trends, in agreement with the major trends of the maps, which are at azimuths of about 035° and 140°. Some of the maps contain other minor north-south trends, many the "band" type just described. Several of the maps (pls. 9, 10, 12, and 13) show a ridge-like resistivity high oriented north-south extending from the origin to 600N or displaced about 100 m to the west.

The "isolation" effect described for the IP maps is also present in the apparent-resistivity maps. Detail in the southwestern quadrant is suppressed on all maps except those with MD 10 as a source electrode (pls. 11 and 14) and, conversely, detail on these maps is lacking in the southwestern, northwestern, and northeastern quadrants. A major northeast-trending resistivity high in the southwestern quadrant is emphasized in the maps where MD 9 was used as a source electrode (pls. 10 and 12) and, although present, is not obvious on the other maps. In fact, upon detailed examination of the six maps, all the major features are present, but their amplitudes, relative levels, and, to some extent, horizontal positions differ markedly according to the different electrode configurations. This phenomenon in mise a la masse measurements is well understood (Ketola, 1972), but this study serves as a good example of the care that must be used both in planning and in interpreting such work in a complexly faulted and fractured area such as the Mahd adh Dhahab district.

Metallic-conduction factor maps.--Maps of the metallic-conduction factor, which is essentially the IP effect divided by the apparent resistivity, are presented for the six electrode configurations in plates 15-20. For the time-domain data the metallic-conduction factor (MCF) was computed from

$$MCF = \frac{IP}{\rho_a} \times 1000$$

where IP is the IP effect in millivolts/volt and ρ_a is the apparent resistivity. In the case of the frequency-effect data, the corresponding MCF was computed from

$$MCF' = \frac{2\pi PFE}{\rho_a} \times 10^5,$$

where PFE is the IP in percent-frequency effect. In construction of the maps, the common logarithm of the MCF, rather than the metallic-conduction factor itself, was contoured because of the large dynamic range of values.

Anomalies in the MCF maps of contour value 2.0 or greater (MCF of 100 or greater) are of interest in the time-domain data, as are values of 4.0 or greater (MCF' of 10,000 or greater) in the frequency-domain values. These values were picked because they include values of both IP effect and apparent resistivity that were considered noteworthy. MCF values greater than 2.0 or 4.0 in the time and frequency domain, respectively, define areas (pls. 15-20) of simultaneously high IP effect and low resistivity and constitute exploration targets. For the most part, these areas have been included in the lists of targets from the IP-effect maps. However, some targets on the IP maps do not appear on the MCF maps because they are resistivity highs. This is to be expected in such a highly silicified environment and such areas are interpreted as zones of disseminated sulfides that are poor conductors but that yield a moderate to large IP effect. The various structural trends pointed out on the IP-effect and apparent-resistivity maps show up rather well, and in some cases are enhanced in the MCF maps. For the most part, these trends are defined by the high MCF values (>2.0 in frequency-domain and >1.0 in time-domain data areas). The MCF maps also show a strong set of east-west trends, especially in the frequency-domain data areas. These trends are due mainly to the isopleths of low MCF values (for example, the 2, 1, and 0 lines) and are due to a combination of the large dynamic range of the MCF values (<1E-2 to >1E+4), the effect of taking the logarithm of these values, and the contour-map generation algorithm used. For MCF values less than 10.0, $\log_{10}$ (MCF) rapidly approaches $-\infty$ so that the gradient of the function $\log_{10}$ (MCF) becomes very steep. The contour map program used here handles very steep gradients by "pushing" the contour lines as close as possible to the defining grid points and thus generating "square corners" and artificial trends parallel to the grid, in this case east-west and north-south. This "square-corner effect" also occurs when a large "single-point" anomaly is present (see, for example, the anomaly at 000, 275E on pl. 8). Although this effect is not serious in the case of "single-point" anomalies, in the case of the MCF maps it generates a spurious set of trends, and isopleths of 2.0 or less in the frequency-domain IP-survey areas and 1.0 or less in the time-domain IP areas should not be used for trend analysis.

Downhole-electric logs

Single-point resistivity and self-potential logs were measured for drill holes MD 8, MD 9, and MD 10 by M. E. Gettings and D. B. Stoeser during the period 26-28 June 1975. The logs were made to locate the optimum positions for the downhole-IP electrodes and to get some idea of the resistivity and self-potential response of the various lithologic units. Holes MD 8, MD 9, and MD 10 were logged to depths of 328.9 m, 393.1 m, and 252.4 m, respectively, using a Neltronic Instrument Corporation logger model 1K, type D. Insofar as was possible, identical procedures were used in logging all holes, including the rate of ascent of the logging electrode. The ground electrode was placed 31 m from the hole collar in a 20-cm-deep pit of mud. The operation of the logger was extensively checked before and after logging of the three holes and was found to be operating properly. The resulting logs are presented in plates 21-23, along with lithologic, mineralization, and structural logs adapted from Worl (1978b).

The same three holes were also logged by ARGAS using a direct current logging circuit with a constant potential; the results are shown in figure 3. The IP electrodes were sited in zones of abundant sulfide concentration at the maximum current positions below 70 m on the logs of figure 3. Note that on the ARGAS logs (fig. 3) the current decreases with depth for holes MD 8 and MD 9, whereas in hole MD 10 it generally increases. After consideration of the available electric and geologic logs, electrode positions were chosen at 104.5 m downhole in MD 8, 194.5 m in MD 9, and 133.1 m in MD 10.

The downhole-electric logs of MD 8 and MD 9 (pls. 21 and 22) can be correlated, as indicated by the numbered correlation points on the two logs. The slight shifts necessary to align the various parts of the resistivity logs are presumably due to local thickening and thinning of units in the section. The self-potential logs also correlate in general, but the SP response of MD 9 was low enough to preclude correlation of particular peaks and shapes as could be done with the two resistivity logs. Given the highly variable nature of resistivities of rocks in this environment, the degree of correlation of the two logs is remarkable and must be regarded as strong evidence that the correlative sections of MD 8 and MD 9 are the same stratigraphic unit.

Correlation of the downhole-electric log for MD 10 (pl. 23) with that of either MD 8 and MD 9 (pls. 21 and 22) is difficult. Examination of the generalized ARGAS logs (fig. 3), however, suggests that the interval 80-160 m in depth in MD 10 might correlate with the interval 130-200 m in depth in MD 9. Comparison of plates 22 and 23 aligned at these zones shows that they are probably correlative, although the correlation is not nearly so convincing as that between MD 8 and MD 9. The inferred correlation points between MD 9 and MD 10 are indicated on plate 23. In any

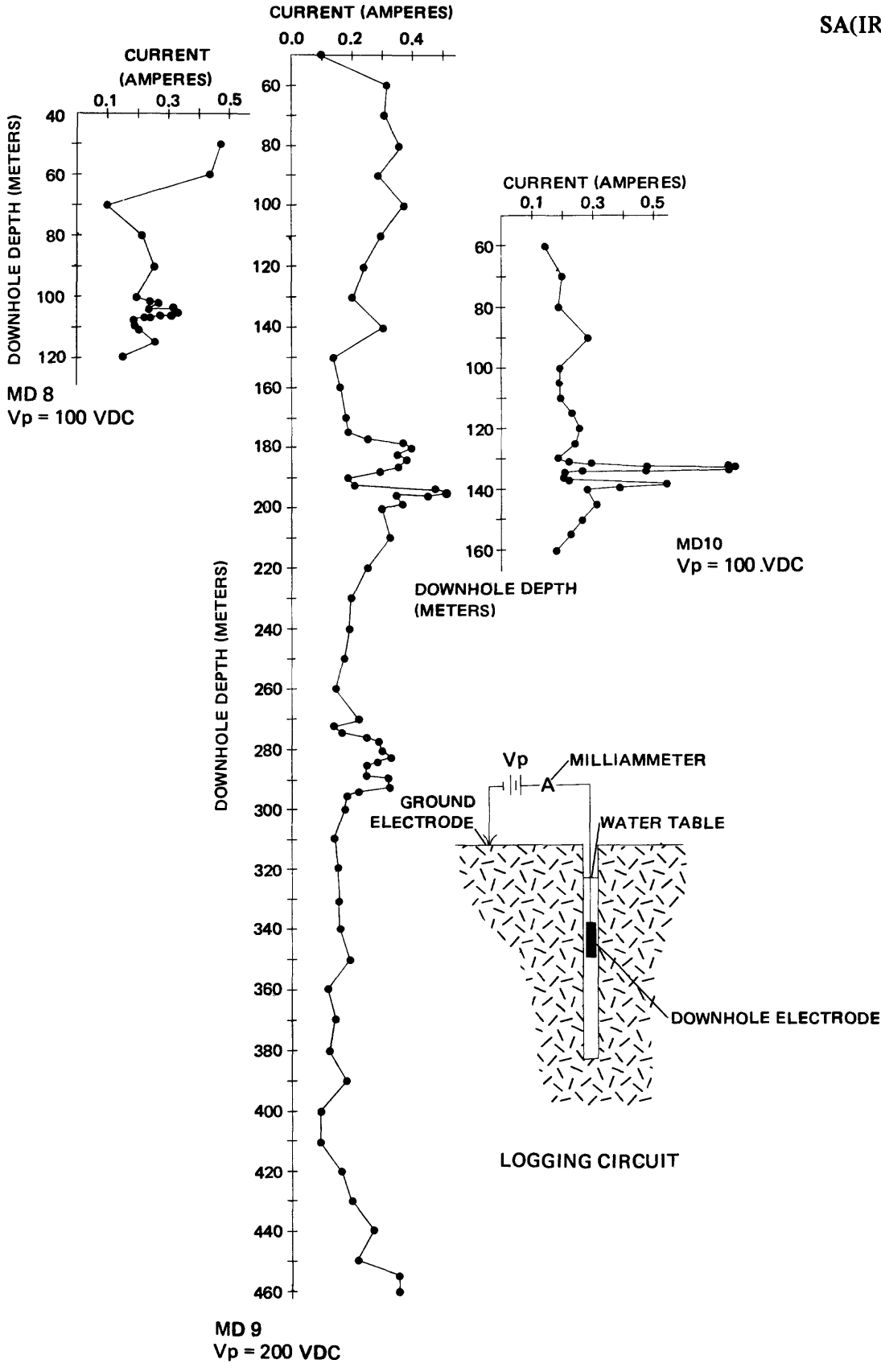

Figure 3.–Direct current electric logs of drill holes MD 8, MD 9, and MD 10 using the logging circuit shown. The logs are positioned along the depth scale so that the parts of the three logs which are believed to correlate are aligned.

case, considerable changes in thickness of responding units appear to be present between MD 9 and MD 10.

Laboratory induced polarization and apparent-resistivity measurements

In order to evaluate the relative IP response of various country rocks and degrees of mineralization, a laboratory study of cores from six samples from the mine dump and from several drill holes was undertaken. Because both the dump samples and drill hole cores were old and unsealed, absolute values of response are meaningless, and only relative comparisons between cores can be made. The IP effect and apparent resistivity were measured using a Scintrex CTU-2 core-testing unit, model 795011 with IP module, and a Scintrex IPR-8 model 726011 IP receiver for instrumentation. All cores were soaked in water for at least 48 hours prior to measurements, and one core (no. 5) was used as a control core and was run before and after each session of measurements. Measurements, most of which were made by M. A. Bazzari but some by M. E. Gettings, were completed during the period 19-29 April 1978. The instruments used yielded measurements of the IP effect at times of 130, 260, 390, 520, 650, 780, 1040, 1300, and 1560 milliseconds after the transmitter current was turned off, and all values were measured over eight complete cycles (pulse on positive, pulse off, pulse on negative, pulse off) of the transmitter. All cores were at least 10 cm long and 2.5 cm or greater in diameter, cut off at right angles ($\pm 15°$) by diamond saw. For each test, current was input at the ends of the core by contact with a felt pad soaked in a saturated solution of copper sulfate, and the response was measured by two copper wire electrodes encircling the core at the center and separated by a distance of 2.54 cm. Contact between the wires and the core is maintained by a cotton wrapping saturated with the copper sulfate solution. For each core the measured quantities were core diameter, current through the core, potential (voltage) between the wire electrodes, IP effect, and contact resistance. The resulting IP-effect voltage decay curves are shown in figures 4-11. The results for all the repeat measurements for dump sample control core 5 indicate the overall repeatability and thus reliability of the experiment. The repeatability is approximately $\pm$ 10mV/V for times before 600 milliseconds, and $\pm$ 5mV/V for later times.

Apparent-resistivity values were calculated for all measured cores using the relations

$$\rho' = \frac{\pi d^2 V}{4LI}$$

and

$$\rho_a = \rho'(1 + \rho_{CT}/300),$$

where d is the core diameter, V is the measured potential

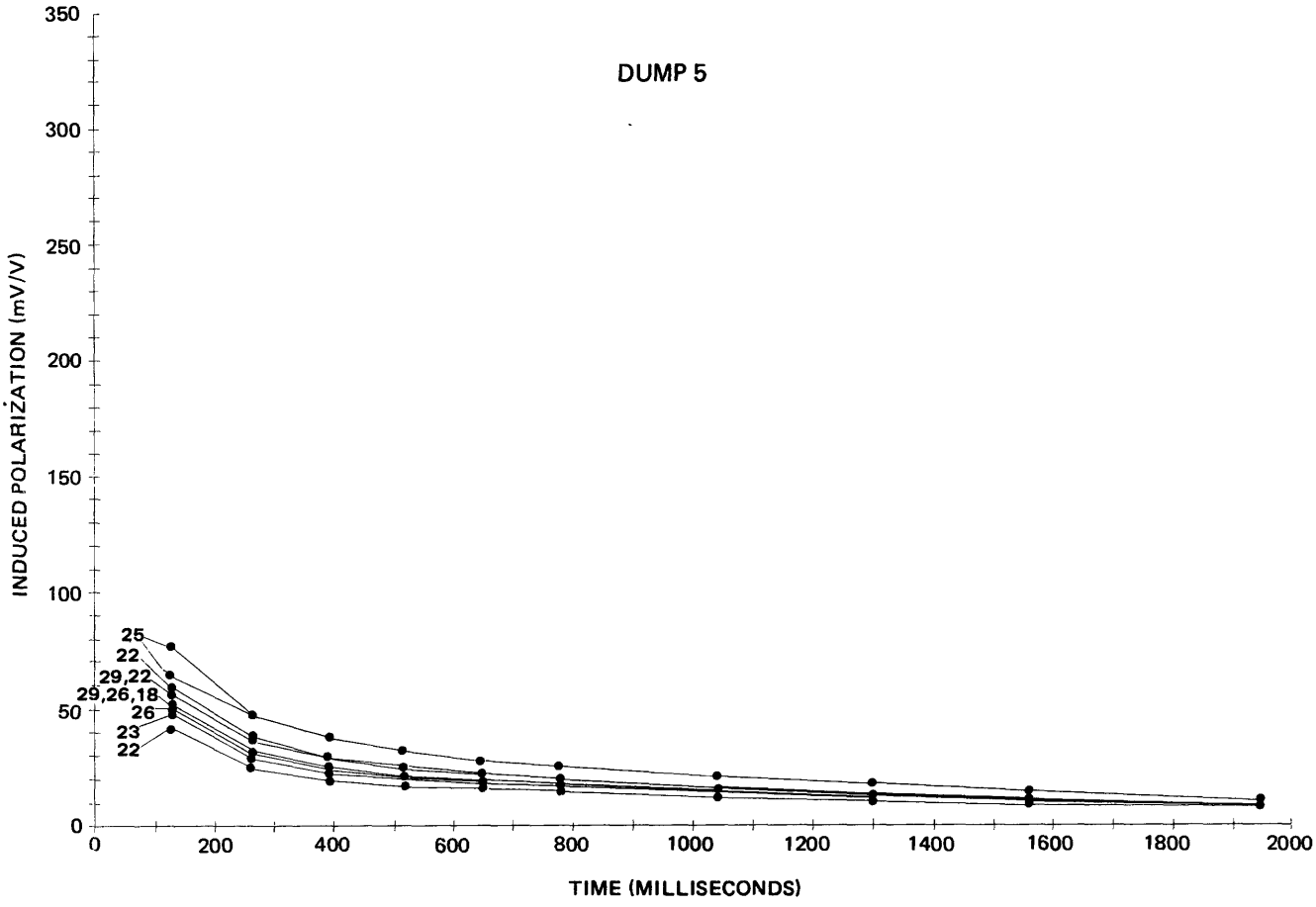

Figure 4.–Observed induced polarization decay curves for the dump sample control core measured at the beginning and end of each session of measurements. (Dump 5, see table 4 for a description of lithology and sulfide content). Numbers labeling curves are the day in April 1978 when the measurement was made.

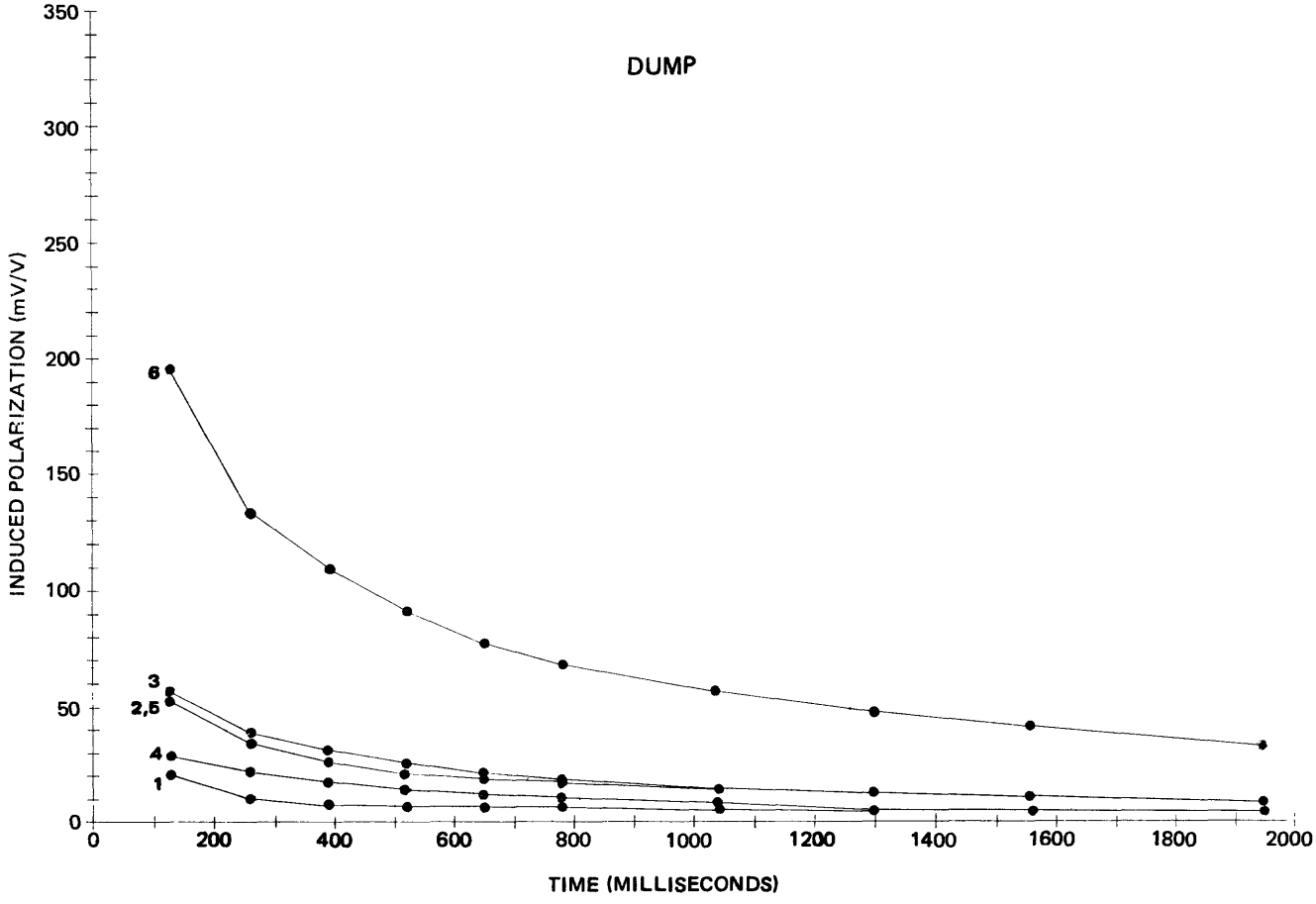

Figure 5.–Observed induced polarization decay curves for cores or six samples collected from the mine dump. The curve of core # 5 is the average of all the curves in figure 4. Lithologies and sulfide contents of cores are described in table 4.

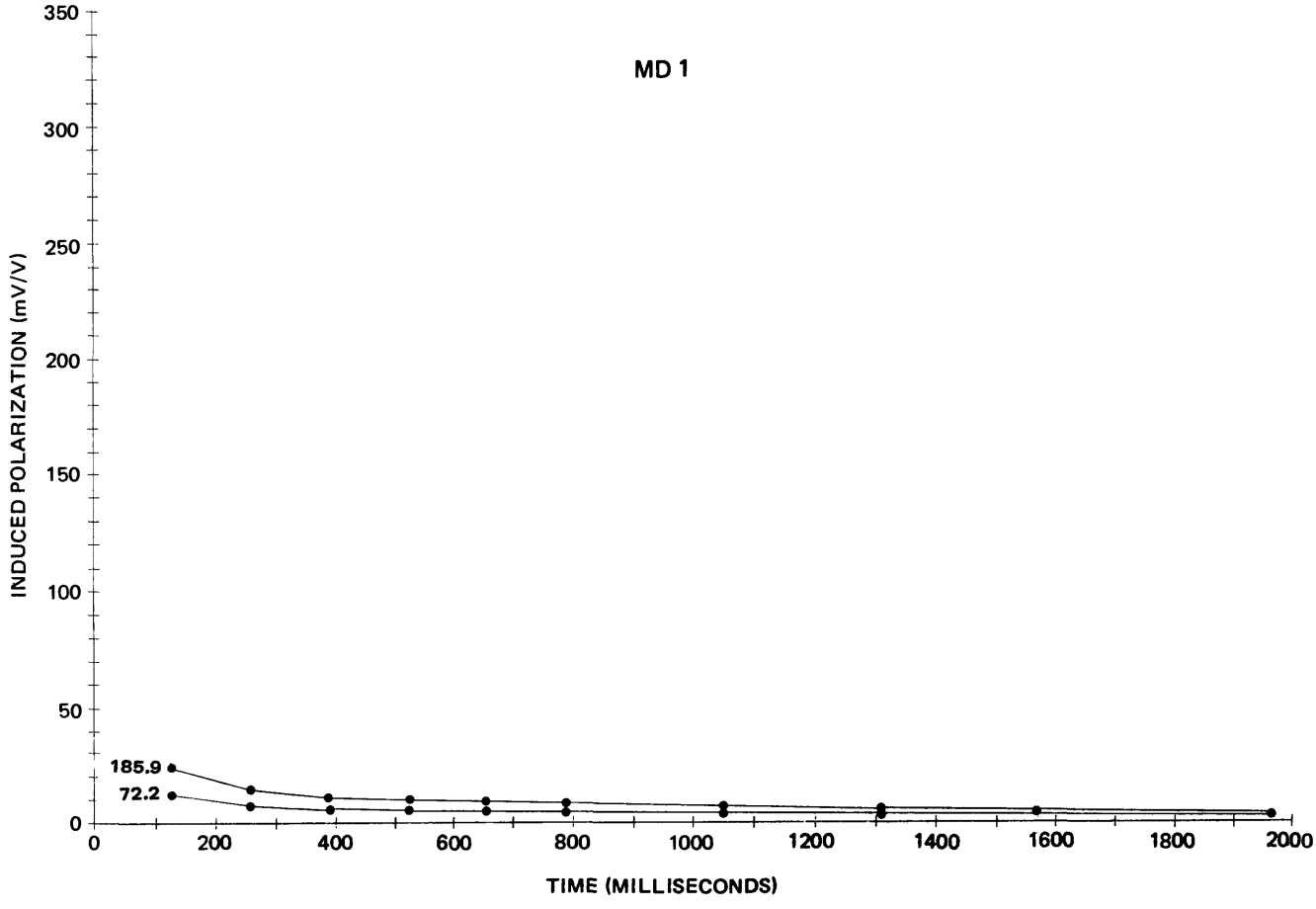

Figure 6.–Observed induced polarization decay curves for two cores from drill hole MD 1. Downhole depth of each core (m) is shown at the left end of each curve. Lithologies and sulfide contents of cores are described in table 4.

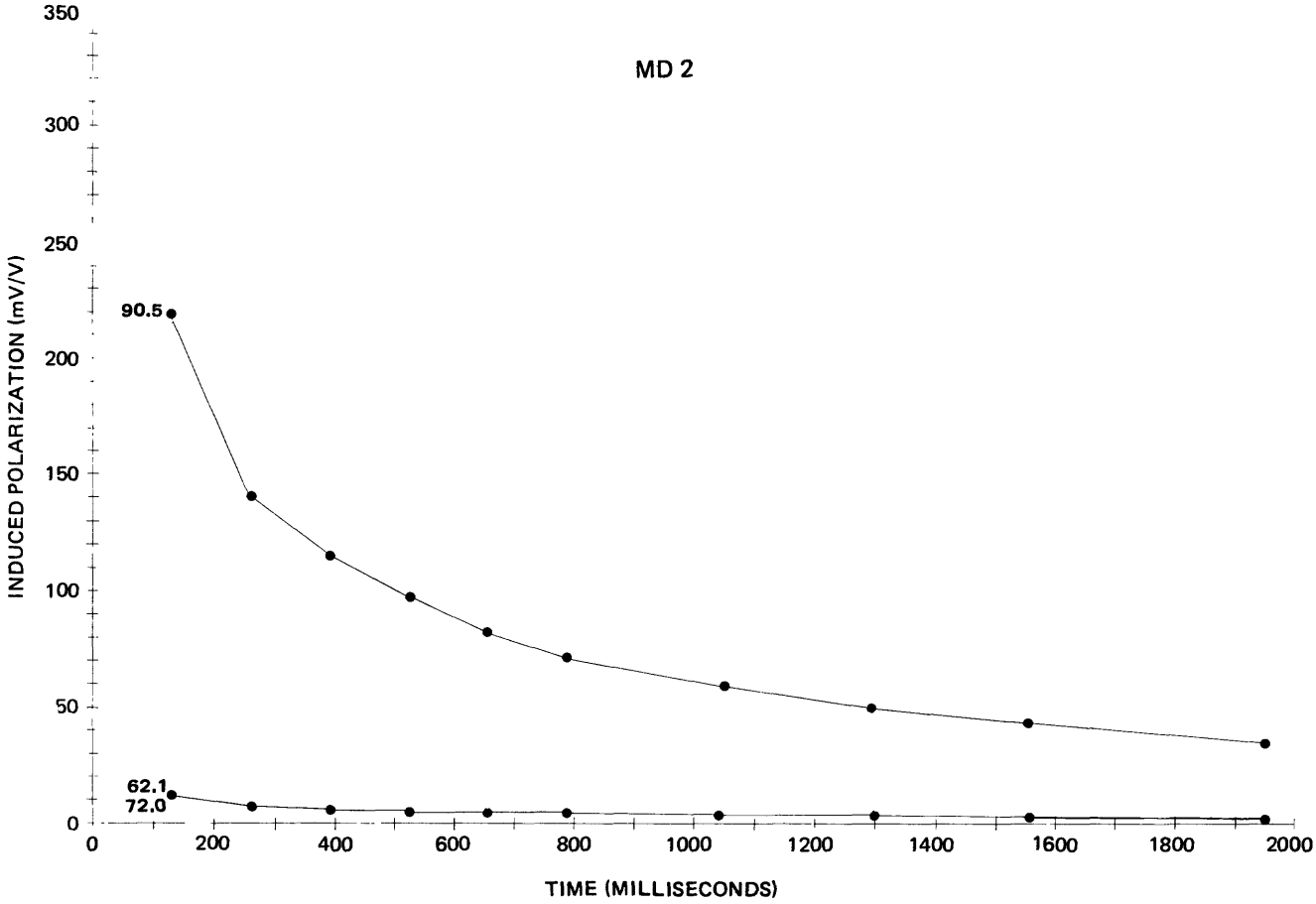

Figure 7.–Observed induced polarization decay curves for three cores from drill hole MD 2. Downhole depth of each core (m) is shown at the left end of each curve. Lithologies and sulfide contents of cores are described in table 4.

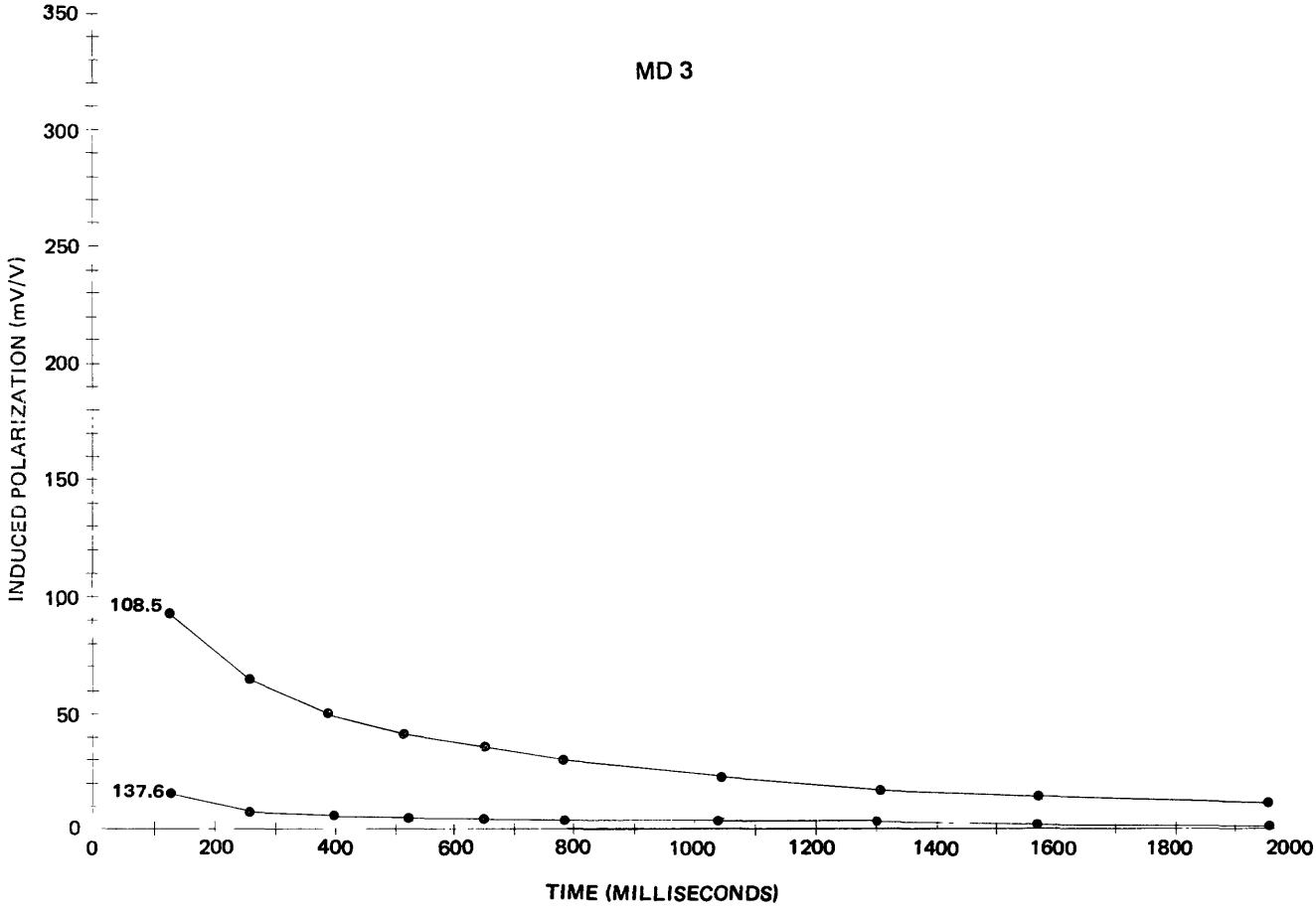

Figure 8.–Observed induced polarization decay curves for two cores from drill hole MD 3. Downhole depth of each core (m) is shown at the left end of each curve. Lithologies and sulfide contents of cores are described in table 4.

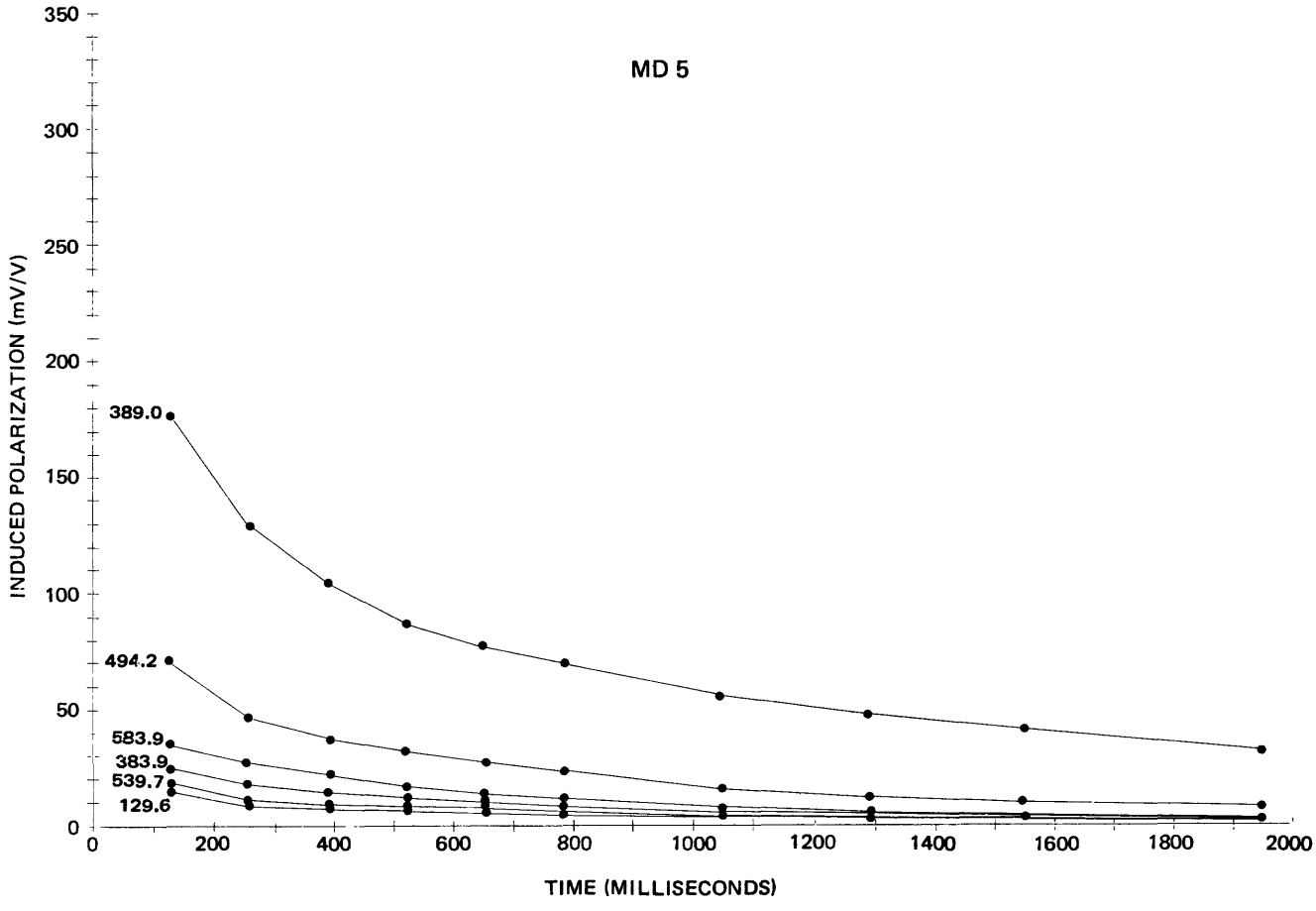

Figure 9.–Observed induced polarization decay curves for six cores from drill hole MD 5. Downhole depth (m) of each core is shown at the left end of each curve. Lithologies and sulfide contents of cores are described in table 4.

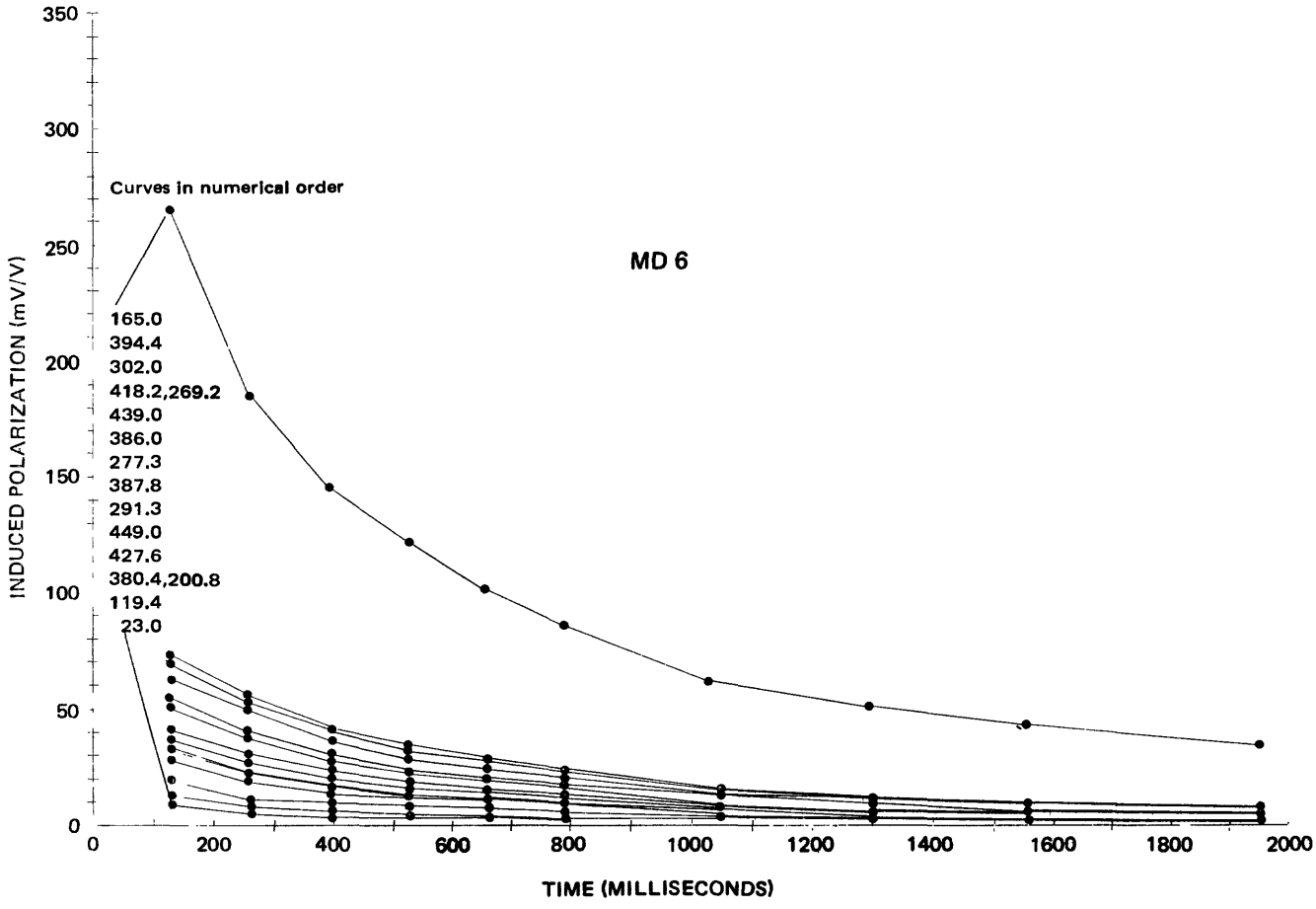

Figure 10.–Observed induced polarization decay curves for sixteen cores from drill hole MD 6. Downhole depth (m) of each core is shown at the left end of each curve. Lithologies and sulfide contents of cores are described in table 4.

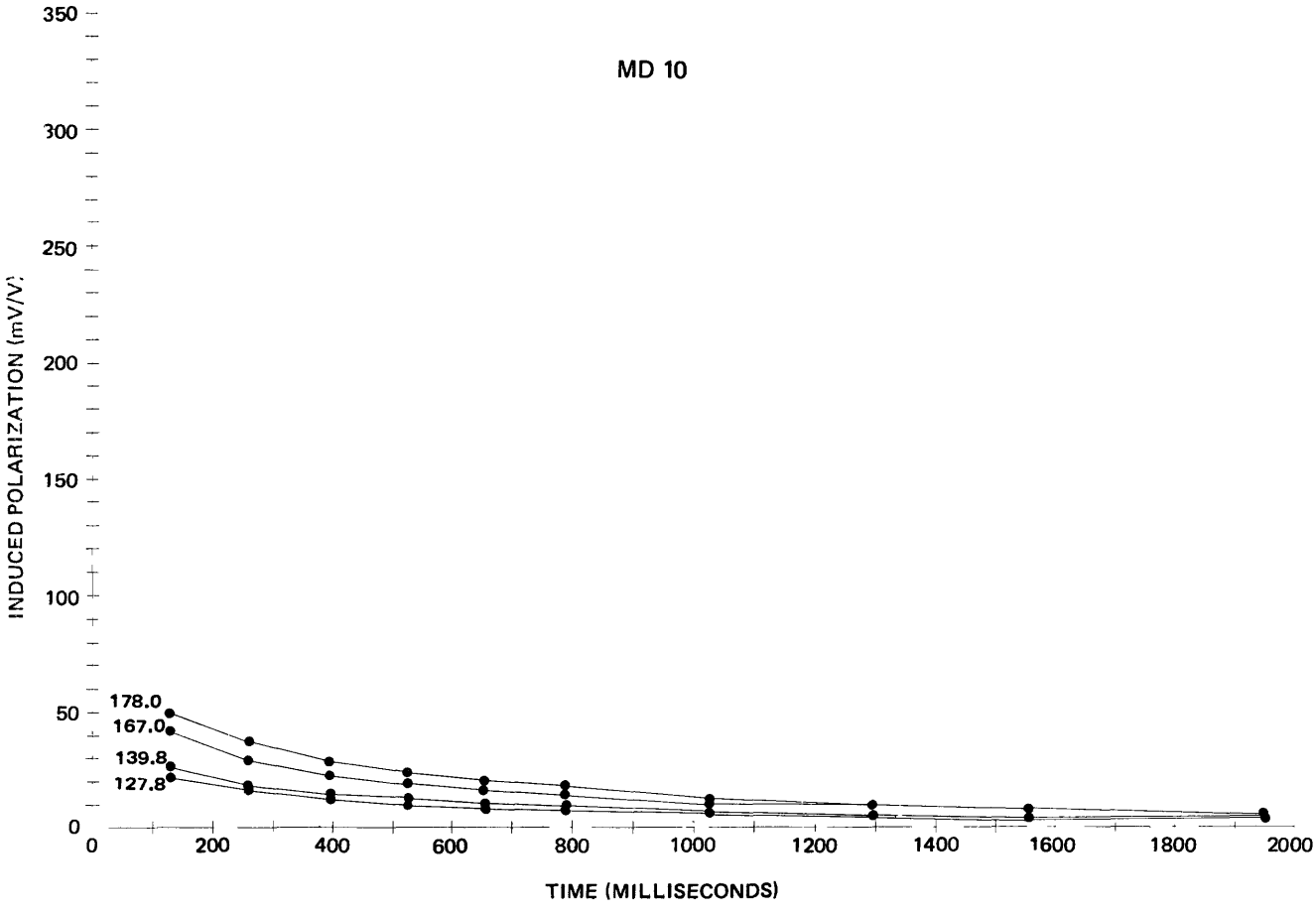

Figure 11.–Observed induced polarization decay curves for four cores from drill hole MD 10. Downhole depth (m) of each core is shown at the left end of each curve. Lithologies and sulfide contents of cores are described in table 4.

difference, L is the spacing between the potential electrodes, I is the current, ρ_{CT} is the contact resistance, and ρ_a is the apparent resistivity.

A commonly used measure of the IP effect is the chargeability, defined as (Telford and others, 1975, p. 708)

$$M = \int_{t_1}^{t_2} \frac{V(t)}{V_o} \, dt,$$

where the quantity $\frac{V(t)}{V_o}$ is the IP-effect voltage decay curve value. Chargeability values were calculated by numerical integration of the curves of figures 4 to 11 between 65 and 1690 milliseconds, after cessation of the transmitter pulse. The results of these measurements are presented in table 4 along with lithologic, stratigraphic, and metallization information. Chargeability values vary from 4 to 158 milliseconds and apparent resistivities from 200 to 59,000 ohm-m. For the 10 measurements of the control core, the mean chargeability was 35 milliseconds with a standard deviation of 7.5 milliseconds, and the mean apparent resistivity was 3040 ohm-m with a standard deviation of 460 ohm-m. These results indicate that the chargeability values have a probable error of approximately $\pm$ 10 percent.

In figures 12a and 12b, the apparent resistivity and chargeability values for the measured cores have been grouped according to the stratigraphic unit from which they came. The most obvious correlation is between the units (see Worl, 1978b) "uat" and "m,q" (q means the core came from a quartz vein), where both the M and a values appear to have a very similar distribution. The chargeability plot (fig. 12b) also suggests that massive sulfide mineralization (that is, large clots of sulfides) that gives high (M>100) chargeability values occurs only in agglomerates or quartz veins. The number of samples in the other units is so small as to preclude any statistical validity for statements regarding their distribution.

The sulfide contents of the cores in table 4 were estimated by visual inspection by M. E. Gettings using a hand lens. These estimates were then grouped into four arbitrary categories of "none", "sparse", "average", and "abundant", and the M and a values were plotted in figures 13a and 13b using these categories as the abscissa. As expected, the average chargeability increases with increasing sulfide content but, surprisingly, M values have a very large variance, and low values are common in the "average" and "abundant" category. This is perhaps due to the rather qualitative nature of the sulfide-content estimates. The distribution of M values in the "abundant" category seems to be bimodal; these modes are interpreted to indicate disseminated (the lower values) versus massive sulfide deposition.

Examination of figure 13b, without regard to sulfide content, reveals that the distribution of resistivities among all measured

Table 4.--*Summary of laboratory induced polarization measurements on samples from the Mahd adh Dhahab area*
[For explanation of stratigraphic unit see Worl, 1978b]

Dump or drill hole sample	Depth (m)	M (milli-seconds)	R (Ω-m)	Strati-graphic unit	Sulfide content	Lithology
Dump 1	-	11	207	-	disseminated (dissem) pyrite, to 3 mm in diameter	quartz (qtz) healed breccia of chloritic material
Dump 2	-	30	13960	-	dissem abundant pyrite, chalcopyrite (chalco), galena, to 2 mm in diameter	qtz-healed breccia; probably originally a lapilli tuff
Dump 3	-	34	9065	-	dissem abundant pyrite, chalco, galena, to 1 mm in diameter	lapilli tuff with many qtz veinlets; much potassium alteration
Dump 4	-	16	14610	-	sparse dissem fine pyrite	lapilli tuff
Dump 5	-	n=10 M=35 σ=7.5	=3039 =463	-	abundant pyrite, chalco, galena, dissem and in veinlets, clots to 4 mm in diameter	lapilli tuff with qtz veinlets
Dump 6	-	125	265	-	abundant galena, minor pyrite, chalco dissem, concentrated along selvages	qtz-healed breccia of of lapilli tuff
MD 1	72.2	7	395	lam	very (v) fine sparse dissem pyrite	lapilli tuff

Table 4.--*Summary of laboratory induced polarization measurements on samples from the Mahd adh Dhahab area* [continued]
[For explanation of stratigraphic unit see Worl, 1978b]

Dump or drill hole sample	Depth (m)	M (milli-seconds)	R (Ω-m)	Strati-graphic unit	Sulfide content	Lithology
MD 1	185.9	14	760	lal	abundant v fine dissem pyrite	andesite, dark-green; carbonate veinlets; contains fragments (frags) of lapilli tuff
MD 2	62.1	7	765	lam	sparse, v fine dissem pyrite	lapilli tuff; hematized; qtz veinlets
MD 2	72.0	7	803	lam	v sparse, v fine dissem pyrite	lapilli tuff; qtz veins; andesite frags
MD 2	90.5	136	10008	-	veinlets and segrega-tions of pyrite, chalco, galena(?), and sphal-erite(?)	qtz vein; vuggy
MD 3	108.5	54	1746	lau	abundant dissem pyrite, chalco, and sphaler-ite(?); sulfides v fine-grained	qtz-healed breccia of chloritic material; tuff; qtz veinlets
MD 3	137.6	7	2795	lau	dissem fine pyrite and sphalerite(?)	
MD 5	129.7	8	1568	uta	none seen	tuff, fine-grained, contains several large frags of lapilli; tuff; qtz veinlets
MD 5	383.9	15	6237	uaa	dissem v fine pyrite	lapilli tuff; potassium-feldspar alteration

Table 4.--*Summary of laboratory induced polarization measurements on samples from the Mahd adh Dhahab area* [continued]
[For explanation of stratigraphic unit see Worl, 1978b]

Dump or drill hole sample	Depth (m)	M (milli-seconds)	R (Ω-m)	Strati-graphic unit	Sulfide content	Lithology
MD 5	389.0	123	1196	uaa	abundant pyrite, chalco, dissem and in veinlets	lapilli tuff, black, carbonate frags
MD 5	494.2	41	58507	uat	dissem fine pyrite and chalco	lapilli tuff
MD 5	539.7	9	2010	uat	sparse dissem fine pyrite and galena(?)	lapilli tuff
MD 5	583.9	20	13863	uat	abundant dissem v fine pyrite	lapilli tuff
MD 6	23.0	4	323	uta	none seen	wacke
MD 6	119.4	8	286	uta	none seen	wacke contains jarosite or similar nonmetallic
MD 6	165.0	158	407	uaa	v abundant, v fine pyrite, dissem, and in veinlets	lapilli tuff, mafics almost wholly replaced by sulfides
MD 6	200.8	9	5659	uaa	dissem fine pyrite	lapilli tuff
MD 6	269.2	36	36783	uaa	dissem fine pyrite	lapilli tuff, qtz veins

Table 4.--*Summary of laboratory induced polarization measurements on samples from the Mahd ådh Dhahab area* [continued]
[For explanation of stratigraphic unit see Worl, 1978b]

Dump or drill hole sample	Depth (m)	M (milli-seconds)	R (Ω-m)	Strati-graphic unit	Sulfide content	Lithology
MD 6	277.3	23	40198	uaa	dissem fine pyrite; chalco veinlets at qtz vein selvage	lapilli tuff, qtz veins
MD 6	291.3	20	1976	uaa	sparse dissem pyrite and chalco; pyrite veinlets along fractures; qtz veinlets	lapilli tuff, qtz veinlets, fractured
MD 6	302.?	41	49520	uat	dissem fine pyrite, galena	lapilli tuff, potassium alteration
MD 6	380.4	10	5290	uat	abundant dissem fine pyrite, chalco	lapilli tuff, potassium alteration
MD 6	386.0	28	31857	m	dissem fine pyrite	lapilli tuff, potassium alteration, silicified
MD 6	387.8	20	25527	m	dissem fine pyrite	lapilli tuff, potassium alteration, silicified
MD 6	394.4	42	50964	m	dissem v fine pyrite	lapilli tuff and fine-grained tuff; potassium alteration; silicified; qtz veinlets

Table 4.--*Summary of laboratory induced polarization measurements on samples from the Mahd adh Dhahab area* [continued]
[For explanation of stratigraphic unit see Worl, 1978b]

Dump or drill hole sample	Depth (m)	M (milli-seconds)	R (Ω-m)	Strati-graphic unit	Sulfide content	Lithology
MD 6	418.2	39	13667	m	dissem v fine pyrite	lapilli tuff and fine-grained tuff; silicified; qtz veinlets
MD 6	427.6	17	879	m	dissem fine pyrite and chalco, along qtz veinlets	crystal tuff; qtz veinlets; fractured
MD 6	439.0	31	34870	m	dissem fine pyrite	tuff, silicified; many qtz veinlets
MD 6	449.0	18	12220	m	dissem fine pyrite	lapilli tuff, silicified; potassium alteration
MD 10	127.8	13	4563	m	dissem fine pyrite abundant in lapilli tuff	lapilli tuff with large frags of silicic tuff
MD 10	139.8	15	4031	m	dissem fine pyrite	lapilli tuff, brecciated; qtz healed
MD 10	167.0	25	10120	m or uat	dissem v fine pyrite and chalco	lapilli tuff, silicified; potassium alteration
MD 10	178.0	28	4381	m or uat	dissem fine pyrite	lapilli tuff, silicified; potassium alteration

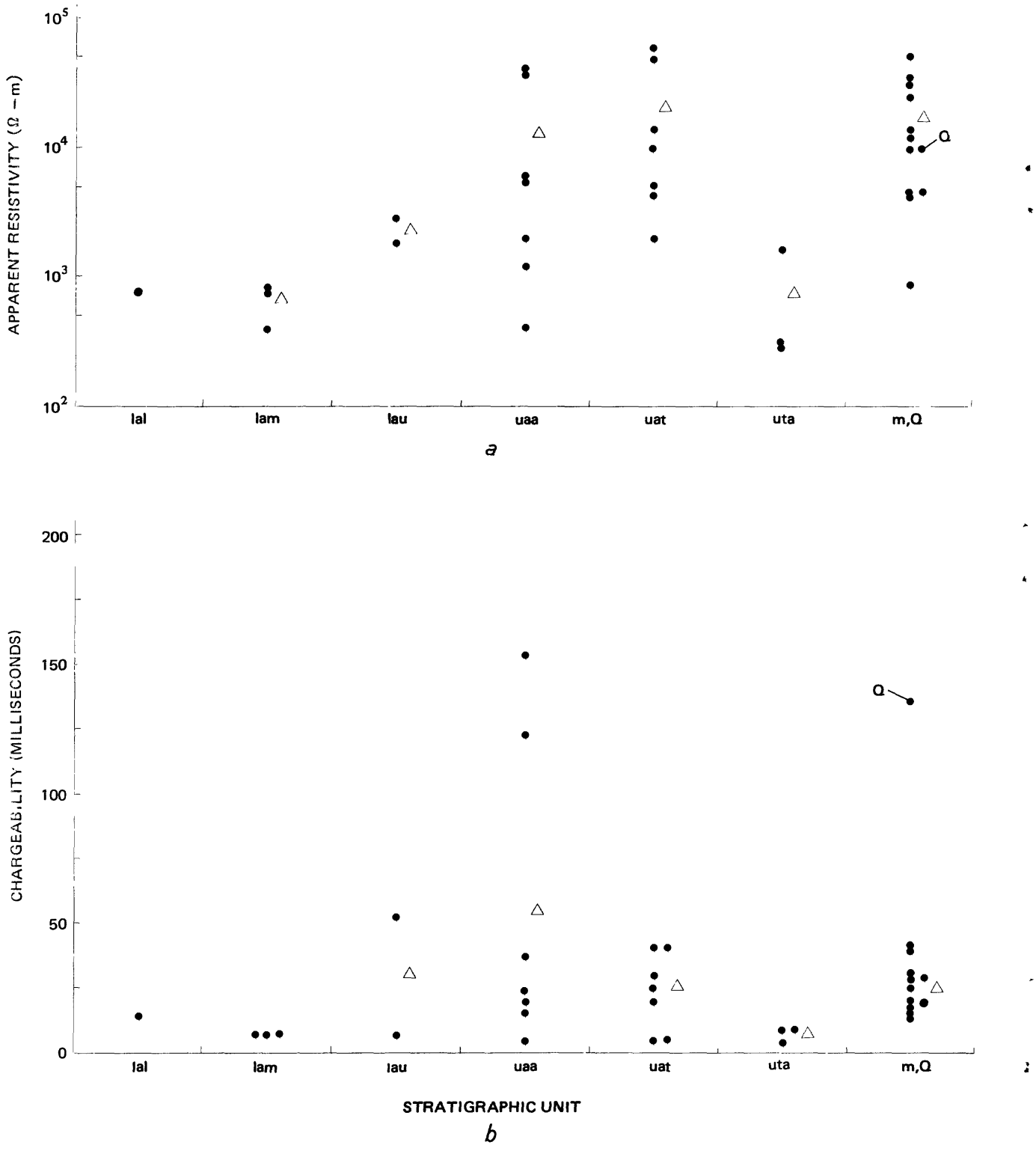

Figure 12a.–Apparent resistivity of cores described in table 4 plotted against stratigraphic unit (Worl, 1978b). The symbol " Δ " is the mean apparent resistivity for samples for each unit. Note logarithmic scale.

12b.–Chargeability of cores described in table 4 plotted against stratigraphic unit (Worl, 1978b). The symbol " Δ " is the mean chargeability for samples from each unit.

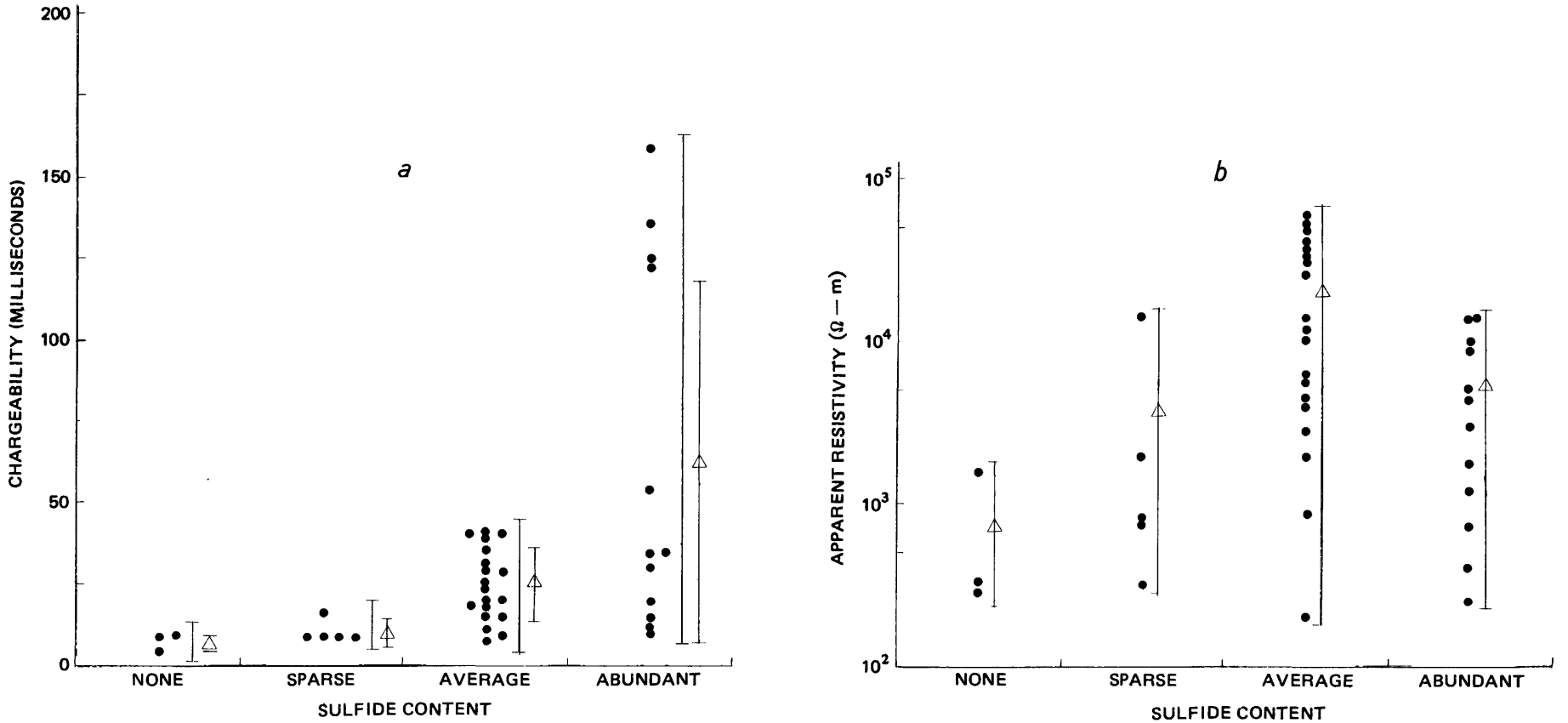

Figure 13a.–Chargeability of cores described in table 4 plotted against sulfide content of cores estimated by inspection. The symbol "△" is the mean for each group and the error bars above and below are one standard deviation in length. Vertical bar shows the range for each group.

13b.–Apparent resistivity for the same cores plotted against sulfide content of cores estimated by inspection. Symbol "△" is the mean for each group and the error bars above and below are one standard deviation in length. Note logarithmic scale.

samples is essentially uniform across the entire range, but with a bias towards the higher values. However, as a function of sulfide content, the average ρ_a value seems to increase overall with increasing sulfide content until the "abundant" category is reached, where the average ρ_a value decreases. For the "none" through lower "abundant" classes, one would expect increasing resistivities because the sulfide mineralization was accomplished via the quartz-veining events and their attendant silicification. Somewhere in the "abundant" category, however, massive sulfide deposition occurs, and the sulfide grains, which are relatively good conductors, become an important percentage of the rock and lower the overall resistivity of the sample.

An alternate method of illustrating the above relationship is shown in figure 14, where apparent resistivity and chargeability have been plotted against each other. In this diagram, it is clear that for chargeabilities less than 100 milliseconds, there is a reasonably good relationship of direct proportion between resistivity plotted on a logarithmic scale and chargeability plotted on a linear scale. In fact,

$$M = 11.0 \ (\log_{10}\rho_a - 2.0)$$

is not a bad estimator for chargeability from apparent resistivity for the samples that contain disseminated sulfide mineralization. This relationship suggests that in the Mahd adh Dhahab district the common exploration criterion of a high metal factor, that is, simultaneous low apparent resistivity and high chargeability, is not necessarily the optimum one. The laboratory work implies that in this case it is probably better to use the resistivity and IP-effect maps and geologic information to deduce the structural controls of mineralization, and then use the IP maps to locate areas of probable sulfide mineralization.

Self-potential survey

Survey description

A self-potential (SP) survey was conducted to map the spontaneous-potential field of the district. The field work was carried out by an ARGAS crew during a 14-day period in August 1975, during which time a total of 1578 points were measured on the 50 m-interval grid extending from 1000 m west to 1500 m east and from 600 m north to 800 m south. Grid points in the area of the abandoned SAMS mill buildings and the open pit area were not measured. Observations were obtained using porous-pot electrodes containing a saturated copper sulfate solution and a BRGM* SP meter of the "PS4" series. The "rectangle method" of surveying was used and five "rectangles" were necessary to cover the area (ARGAS, 1975).

*France Bureau de Recherches Géologiques et Minières

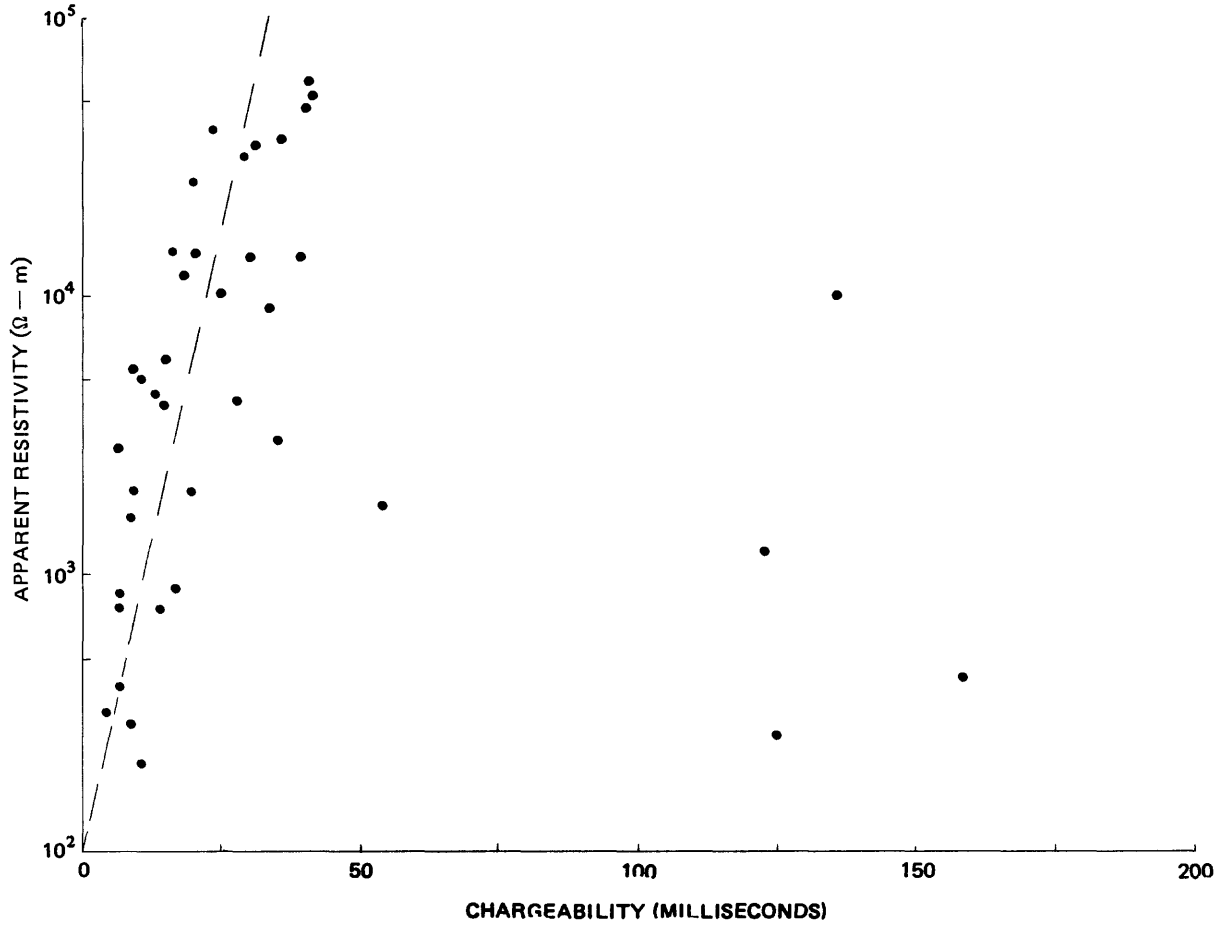

Figure 14.–Apparent resistivity plotted against chargeability for the cores described in table 4. Note logarithmic scale for the apparent-resistivity values. Dashed line is the linear estimation of chargeability as a function of the common logarithm of apparent resistivity. Cores with chargeabilities above 50 milliseconds generally contain massive sulfides; the others generally contain disseminated sulfides.

Data reduction and reliability

The arbitrary zero datum point for the survey is thought to be 300S, 000E, although this is unclear in the report of ARGAS (1975).

No field data sheets were received from ARGAS, so detection of data reduction errors is impossible. Without field sheets, a reliable assessment of the uncertainties in the data is impossible, but from surveys using identical equipment (Blank, and others, 1980) it appears that $\pm$ 20mV is a lower limit for reliability of the data. A 20mV contour interval was therefore chosen for the contouring, since contouring at any finer interval would certainly introduce noise into the map. The SP map (pl. 24) was recontoured by the author from the numbers on the SP map provided by ARGAS (1975).

General features of the SP map

The SP map (pl. 24) is noisy even at the 20mV contour interval; many closed contours are defined by only one point. The distribution of zero contours across the entire area is relatively uniform, so there is no obvious regional SP gradient of which the map is a part. Comparison with the topographic map (pl. 2) shows no obvious consistent correlation between topography or wadi locations and SP anomalies or trends.

Contour distribution in the map is almost entirely controlled by northeast (035°) and northwest (140°) trends, implying that structures trending in these directions are the major contributors to SP response. The large-scale features of the map are: 1) an approximately 1 km-wide belt of predominantly negative SP response whose axis trends about 035° from 800S, 500W to 600N, 500E; 2) a ridge of positive SP response trending at about 120° from the northwestern map corner to 50S, 150E; and 3) east of the negative belt, rather linear northwest-and northeast-trending zones of alternating positive (about 10mV) and negative (about -30mV) SP response.

The largest negative SP anomalies tend to occur at the intersections of the northeast-trending negative belt and the northwest-trending ridge of SP highs. The major SP negative anomalous zones occur in the southern part of the area at 400S to 600S, 050E to 400E and near the western edge of the surface workings at 300N to 400N, 50W to 0. Depth estimates obtained from one-half of the anomaly width at half amplitude for all the major anomalies on the map are in the range of 20-40 m, and where it is possible to estimate dips, they are generally to the northwest. The linear shapes of the individual anomalies in the southern SP-anomaly system imply that they are sheetlike and are controlled by northwest- and northeast-trending fault or shear zones. Since this target area correlates with that defined by

the IP survey, the source is probably sulfide mineralization. The SP-anomaly system on the western edge of the ancient and SAMS workings is also undoubtedly due to sulfide mineralization.

Several other smaller zones of negative SP response of -40mV or greater are present and may be zones of sulfide deposition; however, most are of small horizontal extent.

TURAM electromagnetic survey

Survey description

An electromagnetic survey was carried out over the portion of the grid between 600N and 800S and 900E and 900W using the TURAM method. The field work, data reduction, and plotting of contour maps was done by Habib Merghelani. Field observations were collected during the period 19-25 March, 12-23 April, and 23-24 May 1975 using an ABEM model TURAM TS system. Measurements of inphase amplitude ratio and phase-difference angle were recorded at receiver staff-separation intervals of 40 m down the east-west grid lines.

The transmitter layout was a long wire grounded at each end. The wire was laid in a north-south direction and grounded 1.5 km beyond the edges of the grid, and thus was 4.4 km long. For observations between 200E and 900E, the transmitter line was at 1000E; for observations between 400W and 200E, it was at 500W; and for observations between 900W and 400W, it was located at 1000W. The transmitter, which consists of a motor generator and a control box, produces an output signal of 100-300V at frequencies of 220 and 660 Hz. A current of 1.4 amperes was used.

Data reduction and reliability

For a given receiver spread of 40 m, the so-called reduced-amplitude ratio is computed by multiplying the observed ratio by the ratio of the distance to the nearer receiver coil from the transmitter cable to that of the farther one. The reduced-amplitude ratio is unity for an area where no conductivity contrasts are present (Telford and others, 1975), but will attain values significantly different from 1.0 (for example, 1.4) in the presence of conductors. The reduced-ratio value is plotted at the midpoint of the receiver spread and contoured (pls. 25 and 26). Phase-difference maps can be constructed by simply plotting the measured values and contouring, but this was not done in this study.

The TURAM system used is capable of measuring the phase difference to an accuracy of 0.1 degree and the amplitude ratio to a relative accuracy of 1 percent. Thus the contour interval of 0.1 for the reduced-ratio maps (pls. 25 and 26) is justified.

General features of the TURAM maps

The 660-Hz TURAM map (pl. 25) delineates the shallower conductivity features of the area more sharply than does the 220-Hz map (pl. 26), which tends to reflect the deeper structures. The fact that the major anomalies on both maps are similar in shape and location implies that the conductors extend to some depth and are not just conductive overburden. The major anomaly system in both maps is contained in a north-south band about 300 m wide from 200E to 500 E that extends from 750S to 400N on the 660-Hz map. This system is made up mostly of anomalously high, reduced-amplitude ratio values, exceeding 1.4 in several instances. The individual anomalies trend either northwest (approximately 320°) or northeast (approximately 035°), and the pattern suggests that the conductors are fault or fracture zones of the two trend systems.

Other anomalies occur at: 250N-350N, 900E (reduced-amplitude ratio >1.2); at the western edge of the mine workings (trend 035°, extending from 300N, 0 to 450N, 100E, reduced ratio >1.2); along an east-west zone from 250E to 900E at 650S to 750S (reduced ratio >1.1, anomaly repeatedly cut by 035°, 140° trends); and an anomaly on the 660-Hz map (220-Hz data not taken) at 250N, 660W trending at 010° to the northeast (reduced ratio >1.2).

The lack of substantial, well-defined "negatives" (that is, areas with reduced ratios less than 1.0) on all anomalies implies that the dips of the conductors are steep, probably 60° or greater.

Ground survey of the total-magnetic field intensity

Survey description

A total-magnetic field intensity survey was carried out over the grid from 600N to 800S and from 1000E to 1000W. Observations were taken every 25 m along the grid lines in the east-west direction; lines were 50 m apart in the north-south direction. Three north-south tielines were recorded at 1000E, 00, and 1000W, for checking the consistency and reliability of the data. In all, approximately 2400 observations were recorded.

Measurements were made by means of a Geometrics model G-816 portable proton magnetometer on which the sensor was mounted on a 2.44 m aluminium staff held vertically at each station. An identical magnetometer, on loan from ARGAS, was operated at the base station (140S, 125E), where the total-magnetic field intensity was recorded every 5 to 10 minutes. The sensitivity of the instrument is $\pm$ 1 nanotesla (nT), and at each station a minimum of three readings of the instrument were taken until agreement within $\pm$ 1 nT was obtained. Since the instrument requires 6 seconds per reading, each station required a minimum of about 20 seconds for its magnetic field observation; thus

short-term transients in the data are avoided. Longer period transients are presumably detected in the base station record and removed in the drift correction.

Field work was done by Joseph Adams, M. E. Gettings, and Abdeen Uthman during the period 20-30 May 1975. A suite of 26 oriented rock specimens from the major rock units was also collected for laboratory magnetic-property determinations.

Data reduction and compilation

The data were reduced to an arbitrary datum of 40,000 nT at the base station by plotting the base station readings versus time and reading from the resulting curve the drift correction for any station as a function of time. The corrected station values were then plotted and contoured to yield the total-magnetic field intensity map (pl. 27). As a check on the accuracy of the final values, between-line magnetic field differences measured while doing the east-west lines were subtracted from the same differences measured from the north-south tielines. Of the 49 possible check points in the data set, four were thrown out because they were in areas of steep magnetic gradient where small changes in the sensor head location caused large differences. The differences at the remaining 45 check points have an average value of 0.2 nT and a standard deviation of 2.0 nT, indicating that the data have an overall accuracy of about $\pm$ 2 nT, and that the lines have been successfully brought to a common datum in the map.

General features of the magnetic field map

The district is covered by an aeromagnetic survey (Hunting Surveys Ltd. (unpub. data) 1962) at 150 m terrain clearance and 500 m line spacing. Examination of this map shows that the Mahd adh Dhahab district lies in an area of relatively quiet magnetic response, although it is approximately at the boundary between a magnetically "quiet" zone to the northwest and a "noisy" zone to the south and southeast. The regional trend of the magnetic field map (pl. 27) is from low values in the southwest to higher values in the northeast, and the gradient increases to the southwest. From the aeromagnetic map it appears that this regional gradient is due to the negative portion of a large dipole-anomaly pair of normal polarity, the positive part of which is to the southwest of the map area of plate 27.

Anomalies occur throughout but are most numerous and intense in the southern quarter of the area. Most of the anomalies are due to fault blocks of andesite lava flows exposed at the surface. However, one anomaly, located in the vicinity of 600S, 150E, is buried beneath alluvium, as is the largest (approximately 200 nT) anomaly, whose high is near 100N, 300E and whose associated negative is beneath the mill buildings. Field examinations of outcrops in the area of both these anomalies did not reveal rocks with sufficiently large magnetization to explain the observed

magnetic anomalies. Assuming a normal magnetic polarity and magnetization by induction, standard curve-matching techniques yield depths about 50 m or less and susceptibilities of about 0.002 cgs for the source. Buried fault blocks of andesite are therefore the most likely source, but a shallow level intrusive is not ruled out.

Other anomalous areas of buried sources are north of the mill areas and at 050S, 850E; buried andesite lava flows are once again the most likely source. Another anomaly at 400N, 950W is due to exposed andesitic material.

Trends in the magnetic map are much more variable than those of the electrical maps discussed above, but they nevertheless cluster about the average trends of 035° and 140°. Since the magnetic field reflects the volumetric response of the various lithologic blocks rather than the fracture and shear zones bounding them, the dispersion of trends is not surprising.

The magnetic field, as defined by the 2 nT contour-interval areas (pl. 27) shows considerable detail in the form of offsets and embayments in the contours. In general, these are related to fault and shear zones and demonstrate that the magnetic field map is a geologic mapping aid of considerable utility.

Magnetic properties of oriented specimens

The magnetic properties of a suite of 25 oriented rock specimens taken from the major map units were determined in the laboratory by M. E. Gettings. Specimen locations are shown on plate 1.* An oriented cylindrical core 2.5 cm in diameter and 2.2 cm long was cut from each specimen for laboratory measurements. Magnetic susceptibility measurements were made using a Bison Instruments model 3101A magnetic susceptibility meter. Measurements made with this instrument have an overall uncertainty of $\pm$ 1.5E-6 cgs units. Remanent magnetic intensity vectors were measured using a Schonstedt Instruments model DSM-1 Digital Spinner Magnetometer and a model GSD-1 AC Geophysical Specimen Demagnetizer. Eighteen levels of alternating field demagnetization were applied to each specimen from 25 Oe to 800 Oe. The specimen was demagnetized along three perpendicular axes at each level. No thermal demagnetization was attempted. The DSM-1 spinner magnetometer can measure magnetic intensities as small as 2.5E-8 emu at $\pm$ 5 percent accuracy or better, and determine orientation angles of the intensity vector to within less than 2 degrees. For the tuffaceous rocks, the anisotropic distribution of magnetic materials in the specimen commonly yields standard deviations for the measured remanent magnetization of the order of 20 percent, and thus is the major cause of uncertainty in the measurements, rather than the accuracy limitations of the instrument. The resulting data were analyzed by standard computer methods to estimate the stable magnetic vector directions. Table 5 summarizes the measured magnetic properties.

*Magnetic properties of sample 132002 were not measured.

Table 5.--*Measured magnetic properties of oriented specimens from the Mahd adh Dhahab district*

Specimen	Susceptibility (cgs units)	Konigsberger ratio[1]	Remanent magnetization vector[2] Declination	Inclination	Lithology
132001	4.3E-5	0.53	359	28	Fine-grained silicic tuff
132003	3.5E-5	0.02	354	24	Crystal-lithic tuff
132004	4.5E-5	0.06	160	-50	Silicic lithic lapilli tuff
132005	5.4E-5	-	173	-48	Silicic crystal-lithic lapilli tuff
132006	3.8E-5	15.32	158	-32	Silicic lithic lapilli tuff
132007	2.8E-5	-	348	35	Quartz vein with chlorite stringers
132008	3.6E-5	0.07	357	-11	Fine-grained silicic tuff
132009	3.6E-5	-	359	15	Fine-grained silicic tuff
132010	5.9E-5	0.03	26	-30	Fine-grained silicic tuff
132011	4.4E-5	0.01	174	-57	Silicic lithic lapilli tuff
132012	3.8E-5	-	12	24	Silicic lithic lapilli tuff
132013	6.4E-5	-	214	-50	Crystal tuff
132014	1.9E-6	4.94	185	-34	Silicic lapilli tuff
132015	3.6E-5	0.01	334	15	Crystal-lithic tuff
132016	2.9E-5	0.14	357	37	Silicic lithic lapilli tuff
132017	3.9E-5	0.08	4	-13	Fine-grained silicic tuff
132018	2.9E-5	0.11	8	-25	Fine-grained silicic tuff
132019	5.6E-5	3.00	197	-20	Silicic lithic lapilli tuff
132020	3.8E-3	0.48	339	28	Fine-grained aphanitic andesite
132021	7.8E-5	0.33	357	18	Silicic lithic lapilli tuff

Table 5.--*Measured magnetic properties of oriented specimens from the Mahd adh Dhahab district* [continued]

Specimen	Susceptibility (cgs units)	Konigsberger ratio[1]	Remanent magnetization vector[2] Declination	Inclination	Lithology
132022	1.3E-4	0.19	21	-51	Silicic crystal-lithic tuff
132023	3.4E-5	7.94	270	-10	Silicic crystal-lithic lapilli tuff
132024	3.4E-5	-	357	2	Silicic crystal tuff
132025	3.8E-5	-	357	-52	Fine-grained silicic tuff
132026	5.0E-3	3.27	352	-5	Fine-grained aphanitic andesite

[1] Konigsberger ratio is the ratio of remanent to induced magnetic moments at zero demagnetization level. Ratio is not given if the path of the remanent magnetic vector wandered excessively during demagnetization.

[2] Direction of stable remanent magnetic vector is given by declination (units of degrees, measured clockwise from true north) and inclination (units of degrees, measured positive downward from horizontal into the earth).

The total magnetization intensity values were computed for all specimens whose remanent magnetization did not wander excessively during demagnetization. The value computed was the magnitude of the induced magnetic intensity vector plus the remanent magnetic intensity vector in the stable direction but at zero demagnetization. Most of the total magnetization intensities are in the range of 1E-4 to 1E-5 emu cm^{-3} except for the two andesite specimens (nos. 20 and 26), which are in the 1E-2 to 1E-3 emu cm^{-3} range (fig. 15). In figure 16, profile A-A' from the magnetic field map (pl. 27) is shown together with a theoretical model curve (Andreasen and Zietz, 1969, plate 177) for a flat-topped vertical prism, four depth units along profile by six depth units in the normal direction. The prism extends infinitely deep and is magnetized in the direction of the earth's present field in the district. This particular model was selected by a visual best-fit comparison of the observed and model curve shapes. The quantity plotted on the ordinate is the geometric factor $\Delta T/J_T$, that is, the ratio of the magnetic anomaly to the magnetization per unit volume. For this case, since the peak-to-trough amplitude is $\simeq$50 nT, the anomaly is $\Delta T \simeq 25$ nT, $\Delta T/J_T \simeq 2$, so that $J_T \simeq$ 1.25E-4 is the minimum magnetization necessary to account for the anomaly. This value is shown on figure 15 as the lower dashed line. For the anomaly with maximum at 100N, 300E, for which the negative part is obscured by the mill buildings, $\Delta T \simeq$ 150 nT and the model gives $J_T \simeq$ 1.75E-4 for the minimum volume magnetization. This value is shown as the upper dashed line in figure 15.

Only three of the samples examined have magnetizations larger than or equal to the limits imposed by the model. Of these three, two are andesite specimens (132020 and 132026) and one is a lithic lapilli tuff (132006). The lapilli tuff specimen is composed mostly of andesite fragments, has a remanent magnetization of reverse polarity, and has a suspiciously high Konigsberger ratio. Its magnetization only barely exceeds the lower limit necessary to produce the anomaly of profile A-A'; thus it seems that the andesites are the only rocks studied that are capable of explaining the observed anomalies due to buried bodies. The shallow depths indicated by the steep gradients of the magnetic field anomalies and the absence of intrusive rocks in drill holes or surface exposures considerably restricts the possible geometry of any intrusion causing the anomaly at 100N, 300E. The most likely source therefore seems to be fault blocks of the andesitic material. This explanation is indirectly reinforced by the well log correlation discussed above, which suggests structural repetition of the section in the area.

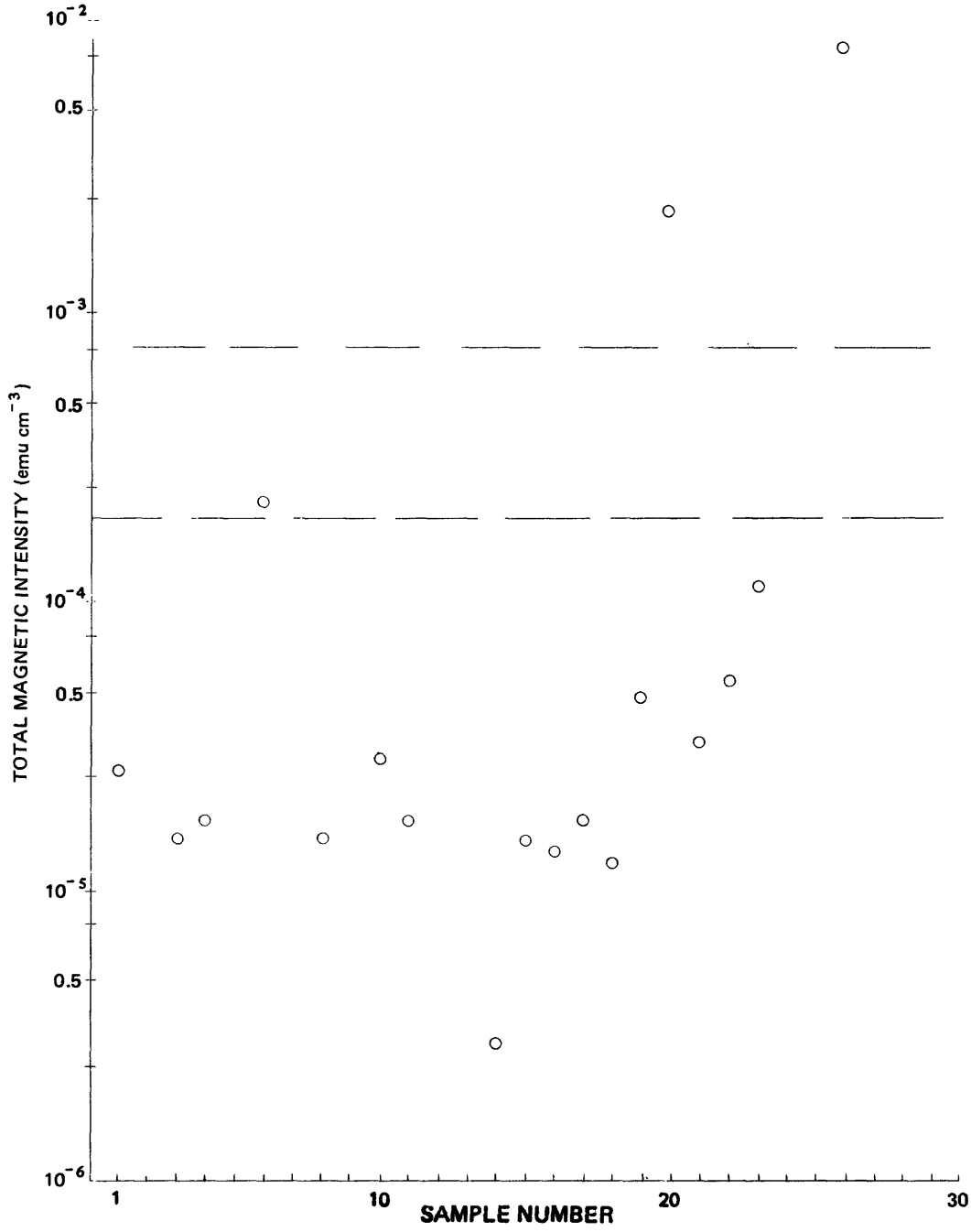

Figure 15.–Distribution of total magnetization intensity (remanent plus induced) for the specimens studied. The horizontal dashed lines are minimum values of total magnetization necessary to produce two observed anomalies in the covered areas. See text for details; note logarithmic scale.

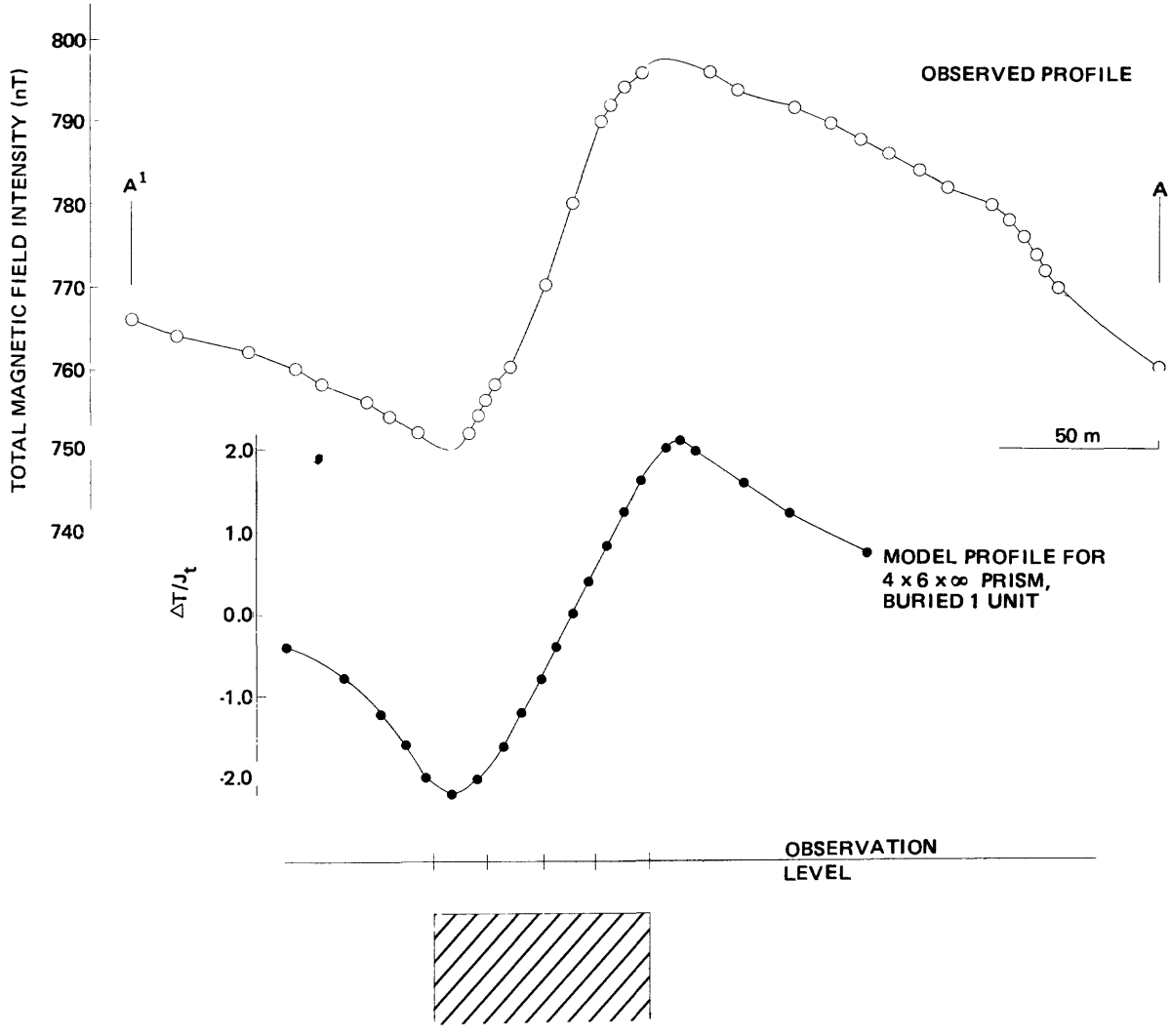

Figure 16.–Observed total magnetic field intensity profile A-A' from plate 27 and a vertical prism theoretical model scaled to fit the observed horizontal and vertical peak-to-trough dimensions. Normal magnetic polarization is assumed; see text for explanation.

Surface gamma-ray spectrometer survey

Survey description

A ground survey of the gamma-ray radiation field was carried out in July 1973 by Khalid Alageel of the DGMR/USGS geophysics department. Data measuring the total count, potassium-40, bismuth-214, and thallium-208 gamma-ray radiation levels were collected. This survey was completed before the 50-m grid was surveyed; thus the lines of the radiation survey do not in general coincide with those of the 50-m grid. The grid used consisted of north-south lines having an interval of 100 m east-west and 40 m north-south; the coordinates of its corners were at 450N, 1229W; 450N, 329E; 550S, 329E; and 550S, 1229W of the 50-m grid. A base station was established at 450N, 379E and was used for the initial and final readings of all data collection intervals. Survey procedure was to go to the base station, calibrate the spectrometer, observe the base readings, proceed westward measuring all stations at the northern line ends until arrival at the line to be measured, proceed southward measuring radiation levels every 40 m (every 20 m in a few places), then proceed eastward measuring the southern-line end stations, and return to base where the closure readings were taken and the instrument calibration checked. Elapsed time to complete a line varied from 2.3 hours for the easternmost to 3.2 hours for the westernmost line. An Exploranium DISA-300 integral gamma-ray spectrometer, set for a 10-second sample time, was used for all measurements.

Data reduction and compilation

The field data were reduced and compiled into individual contour maps of total-count gamma radiation, potassium-40 concentration, and thorium-232 concentration using computer techniques developed by M. E. Gettings (pls. 28, 29, 30). Corrections for instrumental drift, background radiation level, and Compton scattering were applied. Instrumental drift corrections were applied to all station readings by use of timewise linear interpolation between base station readings. Unfortunately, the times of observation of the station readings were not always recorded in the field notes and observation times had to be estimated for most stations under the assumption that speed was constant over the profile.

An arbitrary background correction of 1060 counts per minute (cpm) for total count, 70 cpm for potassium + bismuth + thallium, 30 cpm for bismuth + thallium, and 10 cpm for thallium was subtracted from all readings. These levels were determined by inspection of the data and are the minimum radiation levels for each threshold. The minima for each of the various thresholds do not occur at the same grid point.

In order to accomplish the correction for Compton scattering, the DISA-300 was calibrated in December 1978 by M. E. Gettings using thorium and uranium sources. In addition, sensitivity constants for potassium-40, uranium-238, and thorium-232 abundances

were determined by calibrating the DISA-300 against an Exploranium GR 410 differential gamma-ray spectrometer.

Both Compton stripping ratios and sensitivity constants are available (Geometrics, 1978) for the GR 410, and by taking measurements with both instruments of several granite specimens and the uranium and thorium sources, a calibration of the DISA-300 was accomplished. The resulting stripping ratios and sensitivity constants, along with estimates of their standard deviations, are given in table 6. It should be noted that the instrument was returned to the factory for repair and readjustment twice between the time of the field survey and calibration; the effect of these actions upon the resulting calibration constants and their applicability to this field data is unknown.

The total-count data has a standard deviation of approximately 4 percent, after all corrections, whereas the potassium-40 and thorium-232 abundances each have a standard deviation, after all corrections, of approximately 35 percent. The relatively large standard deviations of the elemental abundances are due to the short sample time interval of 10 seconds that was employed in the survey.

The abundances shown on plates 29 and 30 are quite high, especially the potassium values, which are probably too large by a factor of 5 to 10. This systematic error is thought to be due to instrumental calibration against the GR 410 spectrometer, whose sensitivity constants were measured for assaying specimens placed at the detector. In the field survey, however, the spectrometer was held about 1 m above the ground, and thus the detector samples a much larger volume of rock and registers a correspondingly higher count, leading to high abundance values. The variations in the maps are still valid, however, since the calibration affects only the magnitude of the numbers and not the shape of the mapped surface.

General features of the gamma-radiation maps

The shapes of the gamma-radiation surfaces are best seen by coloring the maps because the data are highly variable and do not produce smooth maps at the survey grid intervals. Many "single-point" anomalies are clearly survey-line dependent. Because of this variability only the general trends and large-scale features are considered reliable in this data.

The major feature of the total-count gamma-radiation map (pl. 28) can be described as a thick zone of generally high gamma-radiation response between two zones of relatively low response, with all three zones folded about a northeast-plunging axis trending approximately 045°. This is consistent with the large-scale structure indicated by the regional mapping of Goldsmith and Kouther (1971). Anomalously high radiation anomalies occur at 250N, 200E; 000, 450W; 300S, 1000W; 100N, 1200W; and in a band

Table 6.--*DISA-300 integral gamma-ray spectrometer stripping equations used to reduce the field survey gamma-radiation data to elemental abundances*

Stripping equations

Th^{232} (ppm) = C_1 (TH)

U^{238} (ppm) = C_2 ((U+TH) - S_1 (TH))

K^{40} (percent) = C_3 ((K+U+TH) - S_2 (U+TH) - S_3 (TH))

where: C_1, C_2, C_3 are the sensitivity constants

S_1, S_2, S_3 are the Compton stripping ratios

TH is the DISA-300 reading in the "TH" position, corrected for background, in counts per minute

U+TH is the DISA-300 reading in the "U + TH" position, corrected for background, in counts per minute

K+U+TH is the DISA-300 reading in the "K + U + TH" position, corrected for background, in counts per minute

Values of constants

Constant	C_1	C_2	C_3	S_1	S_2	S_3
Value	0.272	0.0591	0.0027	3.72	2.46	-3.37
Standard deviation	0.016	0.0033	0.0003	0.17	0.12	0.61

approximately 100 m wide from 250S, 250W to 050N, 150W. Conspicuous areas of low radiation occur in the northwestern corner of the map; at 100N, 150E; at 350N, 150E; in a band from 300S, 550W to 000, 650W; and in a band about 100 m wide from 500S, 650W to 050S, 250W. In general, the radiation lows tend to form more linear anomalies with definable trends, while the high radiation areas are more equant in shape. Anomalies occur both on bedrock and in the alluvium (compare with the base map, pl. 2), and in some cases correlate with wadi courses.

Trends are difficult to define on the gamma-radiation maps, and many consist of apparent lineations of highs or lows on the map or features that seem consistently to interrupt other trends or anomalies along an approximately linear path. The major trends apparent in plate 28 are the linear low radiation areas trending 025° to 045° across the map. Less major trends in the lows are approximately east-west and north-south. The high radiation anomalies define trends that are generally rather short and that have azimuths of about 050°, 140° and a few north-south.

The major feature of the potassium-40 abundance map (pl. 29) is a pattern of a radioactive zone folded about a north- to northeast-plunging axis with nonradioactive zones above and below. A number of areas of anomalously high potassium-40 concentration appear on plate 29, the most conspicuous being a band about 50 m wide trending 090° to 100°, from 450N, 350W to 375N, 150E along the zone of the major surface and subsurface workings; large areas around 100N, 100W and 250S, 050W; and the area around 450S, 800W. Smaller areas of anomalous concentrations of potassium-40 occur at 000, 750W; 100N, 750W; 100N, 1200W; and 200S, 1200W. Comparison of this map with plate 2 shows that parts of several anomalies are due to alluvium in wadi courses that drain anomalous areas; but at least part of all the named anomalies are on bedrock. (Note that beyond 1000W no mapping is available so that anomalies occurring in this area can only be pointed out.) Areas of low potassium concentration occur in a 100-200 m-wide band trending 030° from 350S, 600W to 050N, 300W; in a 100 m-wide band trending about 020° from 100N, 450W to 300N, 350W; in a band trending 090° from 350N, 650W to 350N, 050W; and in the northwestern corner of the map.

As in the total-count map of plate 28, the major trends are in the areas of low gamma-radiation response and are in the directions 020°-035° and 080°-100°. In the anomalously high potassium areas the shape of the larger anomalies suggests northwest- and northeast-trending controls while the smaller areas frequently have east-west trends.

The major pattern of the thorium-232 concentration map (pl. 30) consists of a north-south band about 200 m in width of low thorium concentration from 300W to 500W, with higher abundances in the areas to the east and west. Comparison of plate 30 with

plate 2 shows that the topographically higher areas (bedrock) generally have low values of thorium concentration, while the topographically low areas (mostly alluvium) have higher values. An exception to this is the north-south band 200-m wide at 500W to 700W, which crosses both bedrock and alluvium. This feature may be reflecting a problem with the instrumental data for these lines, but comparison of the tielines across the north and south ends of the survey lines indicates that an anomaly probably exists. Another bandlike high that crosses both bedrock and alluvium occurs from 350N, 200W to 300N, 250E across the zone of the surface and subsurface workings.

The most apparent trends in the map are 070°-120° (mostly defined by areas of low thorium-232 concentration) and east-west and north-south in the areas of high thorium-232 concentration.

During the course of the fieldwork, samples were taken at many of the grid points and subsequently analysed by the USGS-DGMR Chemical Laboratory for potassium, uranium, and thorium contents. Uranium content of the samples was in general below detection limits; thorium ranged from undetected to about 300 ppm and potassium up to 6 percent. Plate 31 is a map of the potassium analyses (as K_2O) drawn by computer methods by Khalid Alageel and V.T. Flanigan. Comparison of this map with the potassium-40 abundance map, plate 29, reveals a remarkable lack of correlation between the two maps, especially in the eastern half of the map where a general negative correlation seems evident.

Considering the high mobility of potassium in the weathering process and the consequent high variability of potassium content at a hand specimen scale, a sampling bias in the specimen is the most likely explanation. Another possibility with interesting consequences for prospecting is that, in the zones of quartz veining, potassium has been mobilized and deposited in zones not readily sampled, for example, in narrow selvages along the veins. The lack of lithologic descriptions for the samples analyzed precludes the testing of either of the above hypotheses.

Shallow seismic refraction profiles

by Habib Merghelani and M. E. Gettings

Survey description

Data from several shallow seismic refraction profiles were collected during July 1973 by Habib Merghelani, Hisham Gazzaz, and Khalid Alageel to evaluate thickness of alluvium and depth of weathering and to locate ancient wadi channels in support of placer gold deposit investigations. An Electro-Tech Porta Seis seismic refraction system composed of one ER-75-12 recording interval timer, 12 EVS-4 miniature seismic detectors (geophones), and an energy source consisting of a truck-mounted 136-kg weight dropped by an electrically operated cargo-release hook was used to measure all profiles. The recorder provides 12 geophone channels with 10 millisecond timing intervals accurate to ± 0.5 milliseconds and records the data on 10.2 by 12.7 cm Polaroid film during an interval of 0.2 seconds. Time breaks for the energy source were obtained by locating one geophone at the shot point.

Locations of the four profiles are shown on plate 2. Profile L3 is an unreversed east-west profile 16.8 m long measured on the alluvium eastward from 460S, 360E to obtain surficial velocities. Profile L4 is an unreversed profile 27 m long measured in the bottom of a trench on the weathered bedrock surface, approximately from 310S, 437E to 289S, 455E, for determination of weathered bedrock velocities. Profile L1 is 305 m long, extending from 414S, 284E to 414S, 589E, and was measured from west to east in four recorder spreads each 76.2 m long. For each spread the energy source was placed at the west end, 26 m east of the west end, and at the east end of the spread, yielding a fully reversed profile. Line L2 is 55 m long, extending approximately from 214S, 403E to 214S, 458E, and was measured in two spreads of 27.4 m each. Both spreads of this line were reversed, but no shot was made in the middle of either spread. A third short profile was measured east-west along 314S, but the data were not reduced.

Data reduction

Arrival times were determined manually from the refraction records and travel-time curves plotted for profiles L1 to L4 by Merghelani. Uncertainty in the measured arrival time is about ± 1 millisecond, due mainly to uncertainties in the location of the time break and the position of the first arrival in the record. The travel-time plots are shown in figures 17 and 18 for profiles L3 and L4 respectively; the travel-time curves for the four spreads (from west to east) of L1 are shown in figures 19, 20, 21, and 22; and the two spreads of profile L2 (from west to east) are shown in figures 23 and 24.

Linear segments of the travel-time curves were defined by inspection, and the resulting slopes and time-axis intercepts were used to compute velocities and depths below shot points for

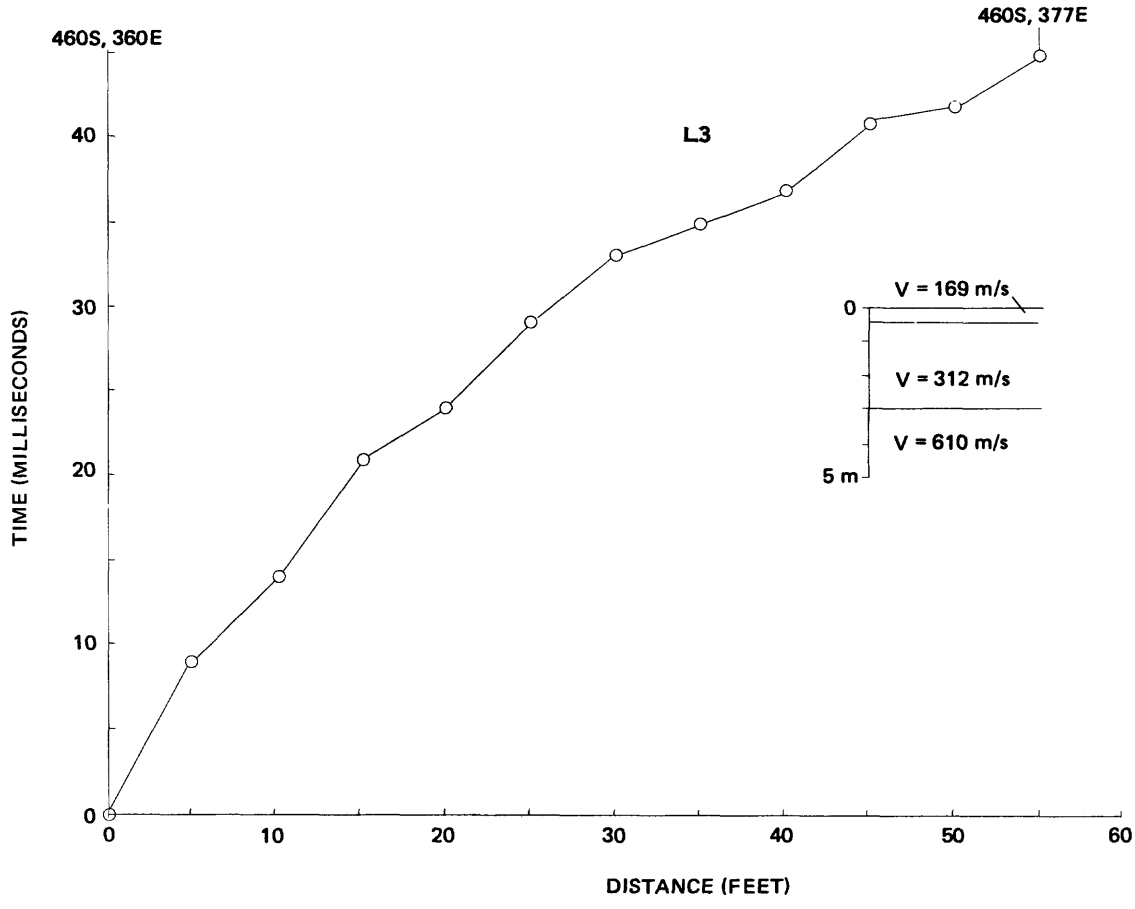

Figure 17.--Time-distance (travel-time) plot for seismic refraction profile L3 and a three-layer interpretation of the curve.

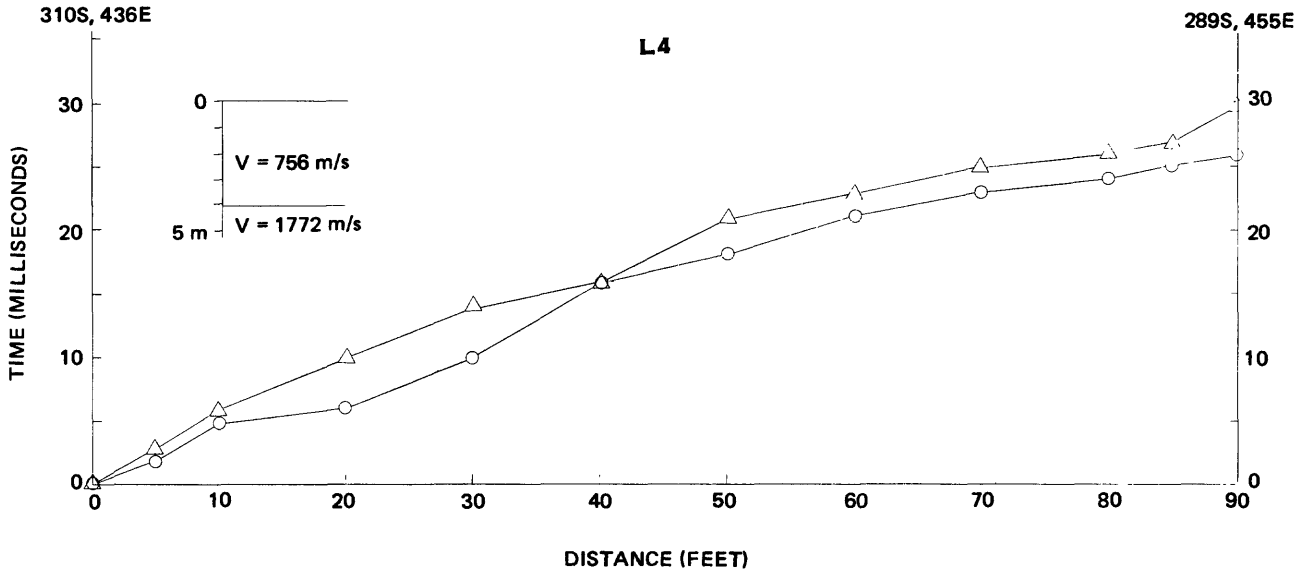

Figure 18.–Two time-distance plots for seismic refraction profile L4 and a two-layer interpretation of the average of the two curves. The profile was measured in a trench in the cover (approx 2 m deep) on the weathered-bedrock surface.

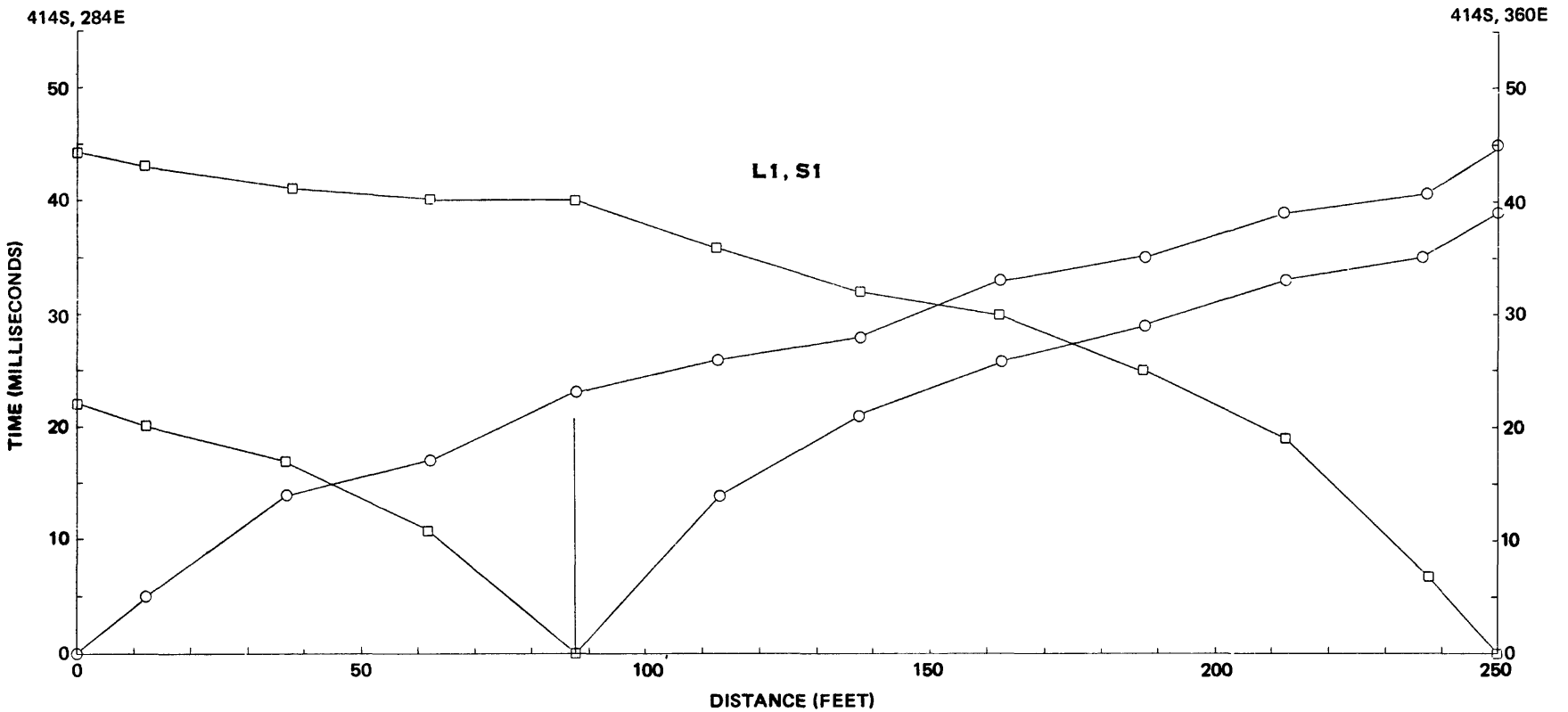

Figure 19.–Time-distance plots for geophone spread 1 of seismic refraction profile L1. See figure 25 for an interpretation.

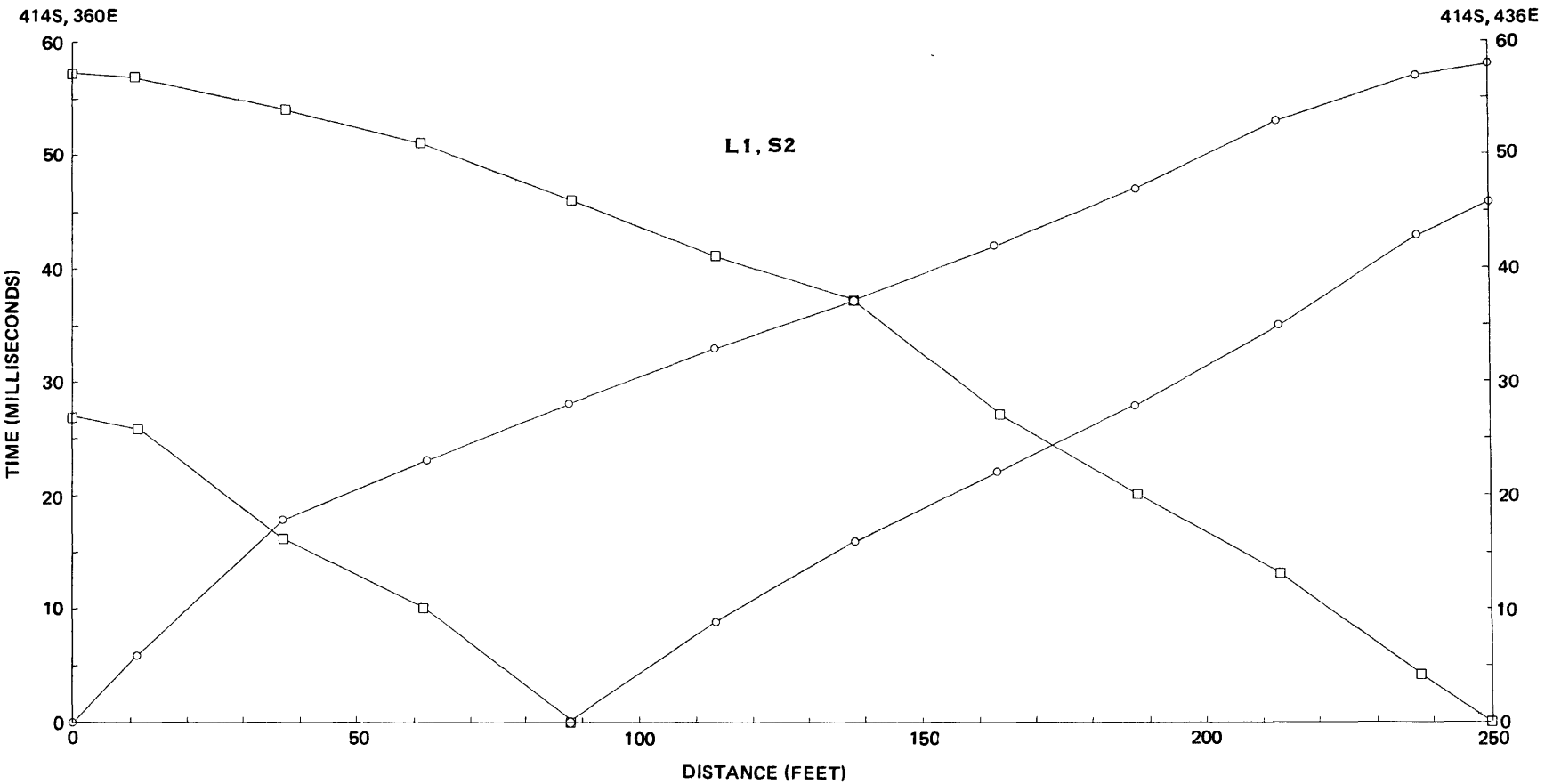

Figure 20.–Time-distance plots for geophone spread 2 of seismic refraction profile L1. See figure 25 for an interpretation.

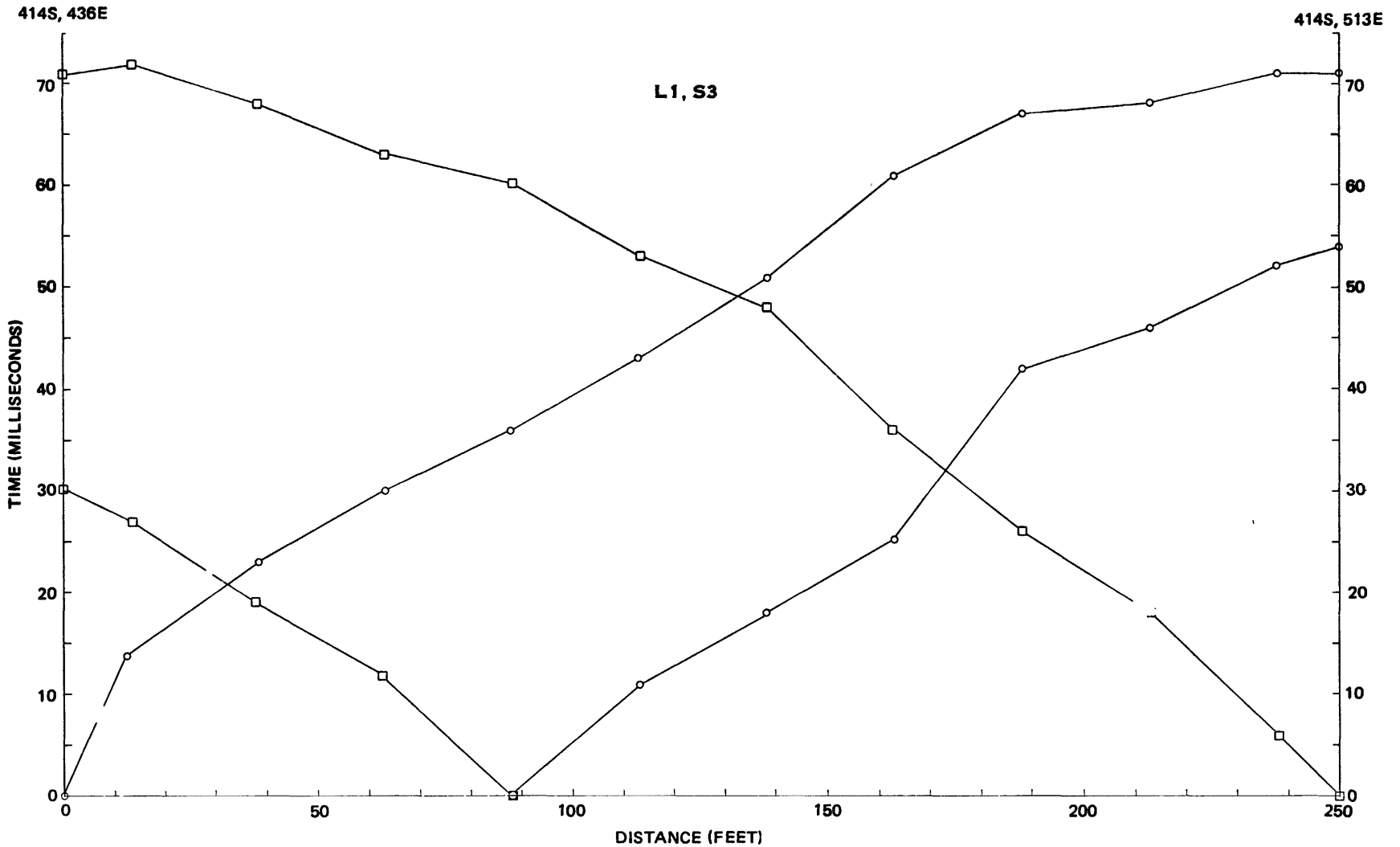

Figure 21.–Time-distance plots for geophone spread 3 of seismic refraction profile L1. See figure 25 for an interpretation.

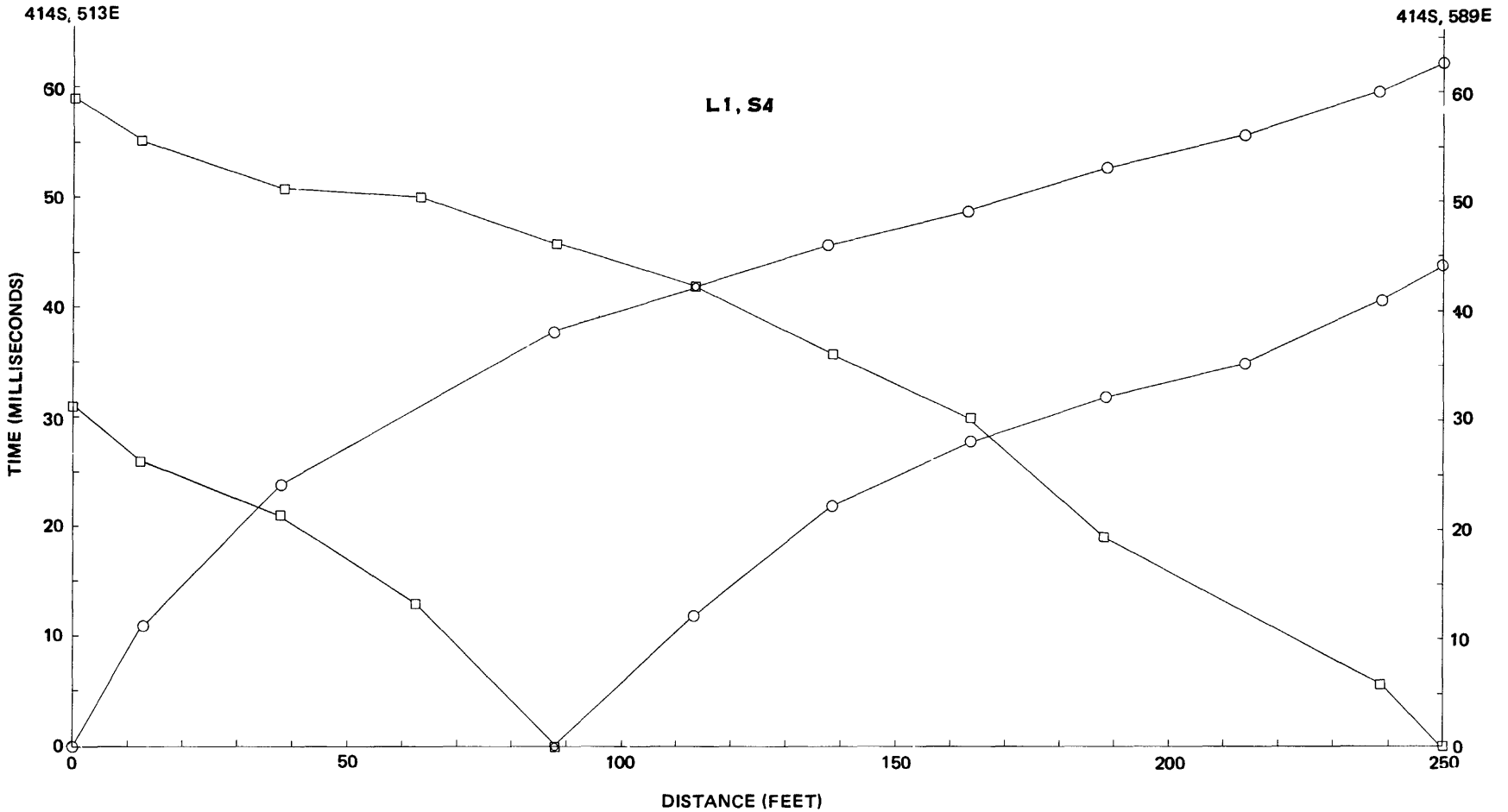

Figure 22.–Time-distance plots for geophone spread 4 of seismic refraction profile L1. See figure 25 for an interpretation.

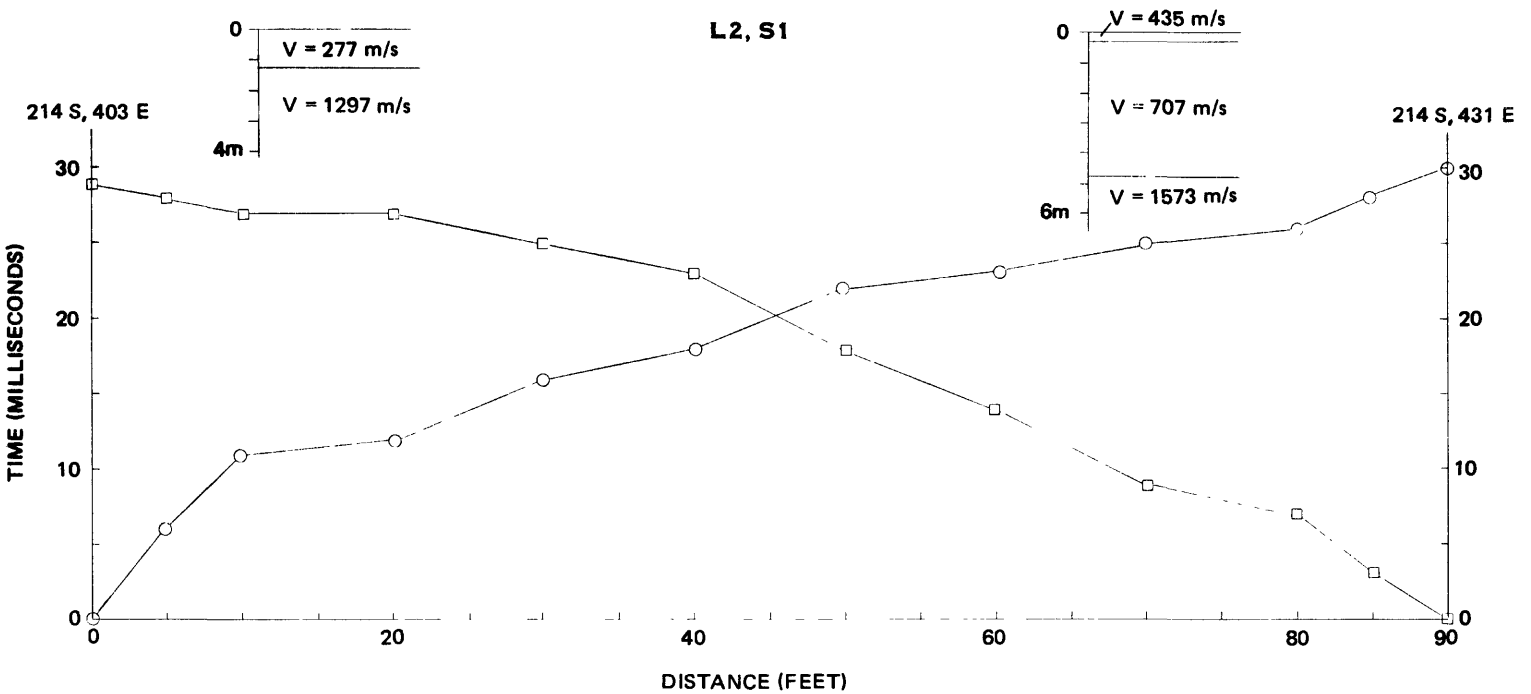

Figure 23.–Time-distance plots for geophone spread 1 of seismic refraction profile L2 with a two-layer interpretation at the west end and a three-layer interpretation at the east end of the profile.

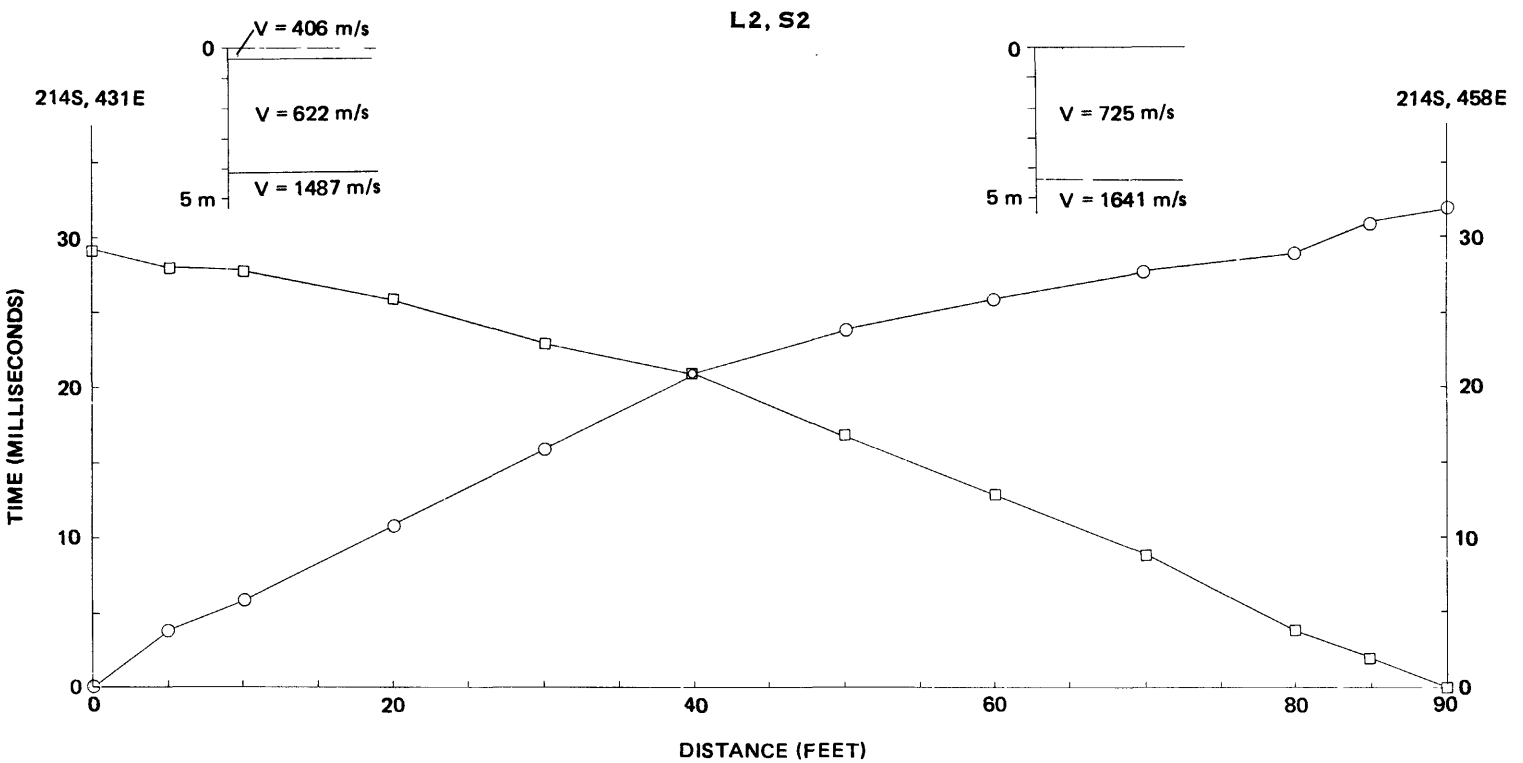

Figure 24.–Time-distance plots for geophone spread 2 of seismic refraction profile L2 with a three-layer interpretation at the west end and a two-layer interpretation at the east end of the profile.

two- and three-layer models by standard formulae. The resulting velocities and depths are shown on the figures. Habib Merghelani, assisted by V. J. Flanigan, used a computer program to reduce the data for profile L1 and to calculate a smoothed-depth interpretation for a three-layer model. The program corrects for elevation variations and the unconsolidated surface layer and computes migrated depths. The model interpretation for profile L1 (fig. 25) shows good agreement with the depth values computed manually beneath the shot points and shows a plausible interpretation.

General features of the seismic refraction profile results

The results of the refraction measurements are reasonably consistent with a three-layer model consisting of surficial alluvium, a layer of weathered bedrock, and bedrock. For the seismic refraction interpretation, weathered bedrock means actual weathered material (that is, a saprolitic surface) and not necessarily the underlying bedrock, which may have undergone chemical alteration but not have a significantly lowered seismic velocity. The surface layer of alluvium has an average velocity of about 300 m sec^{-1} and generally has a thickness of one-half to three meters. The seismically determined surface-layer thickness agrees well with thicknesses determined by trenching (Bagdady and others, 1978) in areas where they can be compared. The second layer (weathered bedrock) has a velocity of about 600-700 m sec^{-1} and is about 4 m in thickness. Layer three has a velocity of about 1600 m sec^{-1} and probably represents the deeper parts of the zone of weathering. The computer solution, which is corrected for the alluvial surface layer described above, also consistently resolved a refractor of about 2400 m sec^{-1} velocity at 5 to 30 m depths. The 1600 m sec^{-1} and 2400 m sec^{-1} layer velocities are characteristic of sandstones and shales (Grant and West, 1965, p. 8), to which the volcaniclastic rocks of the district are probably comparable. The boundary between layer 2 and layer 3 of figure 25 is probably not the water table, since it is 40 to 70 m or more below the surface everywhere and its predicted elevation projected from drill hole MD 8 is about 1015 m at the west end of L1. It is improbable that the water table is perched in the alluvium of this area. Thus, unless there is a zone of the weathered layer of about 1600 m sec^{-1} velocity, which seems unlikely here, the layer-three refractor probably represents a lithologic change. The classic response (Heiland, 1940, p. 515-517) of a normally faulted and subhorizontal layered section is shown in the travel-time curves of figures 19-14. Because of the gravity evidence (see below) and because all of the layers in general thicken and thin simultaneously, the interpretation of figure 25 in terms of faulting seems the most likely model.

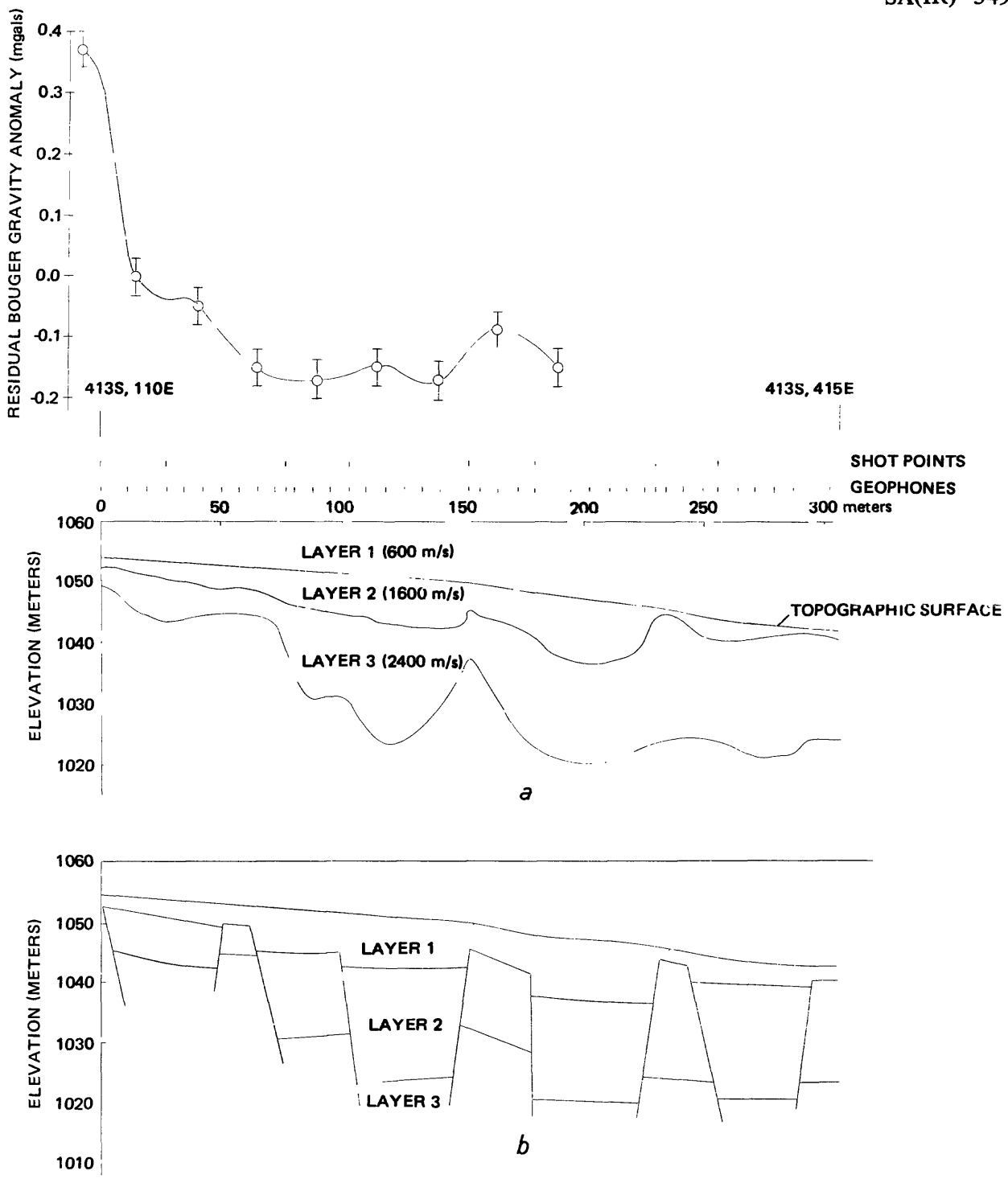

Figure 25a.–Residual Bouguer gravity anomaly along profile L1 and a computer-generated three-layer interpretation of the time-distance curves for the four geophone spreads of seismic refraction profile L1 (figs. 19-22). Locations of geophones and shot points are shown above the topographic profile.

25b.–A fault interpretation of the combined gravity and seismic data of *a*. Dips of fault planes are schematic.

Gravity survey of the southeastern part of the district

Survey description

A gravity survey of the pediment and alluvial plain in the southeastern part of the district was carried out by Hisham Gazzaz and Habib Merghelani on 4 July 1973 between the hours of 0430 and 1605 GMT.* A total of 170 stations including the base station were measured during this period using LaCoste and Romberg gravimeter G-138. Gravity station locations were surveyed to a relative vertical accuracy of $\pm$ 1 cm or less and relative horizontal accuracy of $\pm$ 9 m or less. The grid consisted of 10 east-west lines spaced 100 m apart in the north-south direction and a grid-point spacing of 25 m east-west. The corners of the grid are located at 014S, 075E; 014S, 475E; 914S, 075E; and 914S, 475E. The survey began with the northernmost line and finished with the southernmost, and the base station was read at 0430, 0912, and 1605 hours GMT.

Data reduction and reliability

The data set was reduced to simple Bouguer gravity anomaly values by means of a digital computer program (Godson, 1974). After correction for earth-tidal effects, the drift rate of the gravimeter was 0.0017 mgals per hour for the period 0430-0912 GMT and 0.0075 mgals per hour for the period 0912-1605. Thus even if all the drift is attributed to one station, the maximum error in relative observed gravity is 0.05 mgal or $\pm$ 0.03 mgal.

Considering the uncertainties in relative observed gravity, latitude, and elevation, a standard propagation-of-errors treatment (Bevington, 1969) yields an estimated standard deviation of $\pm$ 0.03 mgal for the simple Bouguer gravity anomaly values and implies a minimum contour interval of 0.05 mgal for this data set.

The simple Bouguer gravity anomaly map is presented in plate 32A. It should be noted that where a contour falls along an east-west line of stations, the contour "wobbles" with an amplitude of about $\pm$ 0.03 mgal and verifies the error analysis above. Furthermore, because of the unequal grid spacing (100 m north-south and 25 m east-west) the map is directionally biased, so that it shows more detail in an east-west direction.

General features of the gravity anomaly maps

The simple Bouguer gravity anomaly (SBA) map (pl. 32A) shows a northward-decreasing gravity field at an average rate of about 1.6 mgal/km. The central half of the map shows a complex north- to northeast-trending anomaly consisting of a central high flanked by lows. In the southeastern corner of the map an

* Greenwich mean time.

isolated high anomaly has a distinct northeast-trending gradient, and generally low values in an east-west trend on the northern edge of the map seem to truncate the north-trending high in the center of the map. The northwestern corner of the map contains a hint of northwest trends, which are generally lacking in the rest of the map area.

Station elevation and SBA are plotted versus east-west position, in figure 26, for the three lines nearest high topography in order to evaluate the correlation between elevation and SBA. The minimal correlation suggests that, as expected in this rather flat terrain, the Bouguer slab correction accounts almost totally for terrain variations within the map area. The large (approximately -0.4 mgal) negative anomaly on the southern profile could be explained by an elevation error of about -2 m. However, an SBA minimum of lesser amplitude would still be present and the shape of the map would not be greatly altered.

In order to define the local features of the anomalous gravity field, the regional trend was removed by fitting a least squares plane to the SBA grid, subtracting the plane from the SBA, and drawing a contour map of the residual values. The plane removed has the equation

$$P(x,y) = (-90.53 - 1.040E\text{-}4\ x + 1.760E\text{-}3\ y)\ \text{mgals},$$

where x is the distance in meters east from (014S, 075E) and y is the distance in meters south from the same point. The residual map is shown in plate 32B at a contour interval of 0.05 mgal. Again "noise" is present on controlled east-west contours to the extent of about $\pm$ 0.03 mgal, but the map as a whole is reasonably smooth.

The residual gravity anomaly map (pl. 32B) shows a northeast-trending high of about 0.3 mgal in the southeastern corner of the map that has well-defined gradients to the northwest and to a lesser extent to the southeast. The central part of the map shows linear north- to northeast-trending highs flanked by linear lows. The highs are truncated about 200 m from the northern edge of the mapped area. Structural controls for the gravity anomaly sources are suggested by north-south, 035°, and 140° trends in the residual gravity field.

QUALITATIVE INTERPRETATION OF THE GEOPHYSICAL DATA

Introduction

The major emphasis of the interpretation has been to define and explain correlations among the data sets from the various geophysical surveys and between the data sets and the geological and geochemical data. The primary objective was to delineate target areas of sulfide mineralization. Also, an effort has been

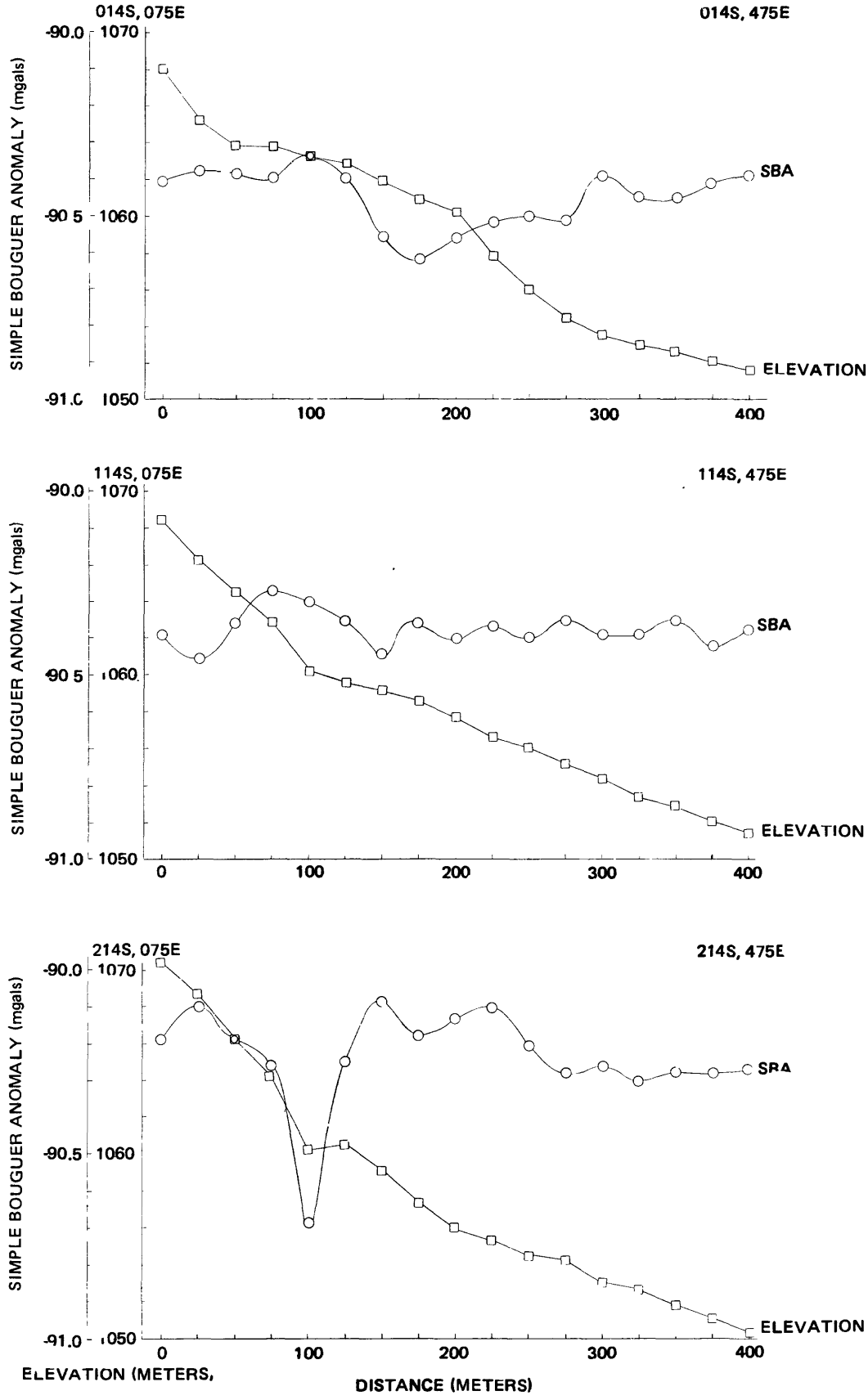

Figure 26.–Plots of topographic elevation and simple Bouguer gravity anomaly (SBA) for the three northernmost profiles of the gravity survey.

made to derive a structural model consistent with the constraints of all the data. Results of the interpretative work are presented in an order beginning with those pertaining to restricted areas and shallow depths, and progressing to those covering larger areas and greater depth of penetration.

Near-surface features

The travel-time curve of refraction line L3 (fig. 17) reveals the near-surface structure of the alluvium. This line was oriented east-west, 16.8 m in length, and had a geophone spacing of 1.5 m. Interpretation of the travel-time curve using a three-layer model yields an upper layer of 0.5 m thickness with a velocity of 169 m sec^{-1}, a second layer 2.5 m thick with a velocity of 312 m sec^{-1}, and a third layer velocity of 610 m sec^{-1}. From trenching work in the immediate area (Bagdady and others, 1978), the unconsolidated cover seems to be about 1 to 3 m in depth, and line L3 appears to be resolving two layers in the unconsolidated material: first, a thin layer of loose cover (perhaps with a high percentage of windblown sand) in layer 1; second, the bulk of the unconsolidated materials (for example, transported material) in layer 2; and finally, weathered bedrock in layer 3. The measured apparent velocities listed above fall in the ranges for the types of materials suggested (Heiland, 1940, p. 468), and thus support this interpretation.

Refraction line L4 (fig. 18) was measured along the bottom of a trench on the weathered bedrock surface along a 27.4-m profile with a 3.05-m geophone spacing except at each end where an intermediate geophone was placed at 1.52 m. The profile was measured twice, and both of the resulting travel-time curves were interpreted with a two-layer model, although the curves suggest a three-layer model could also be attempted. The results were a layer of about 4 m thickness and average velocity of 760 m sec^{-1} overlying rock with a velocity of about 1770 m sec^{-1}, the upper layer being in good agreement with layer 3 of line L3. Combining these results with those of line L3 suggests that the variations in the velocity of the upper part of the weathered bedrock is likely to be of the order of $\pm$ 15 percent.

Interpretation of profile L2 (figs. 23, 24) suggests that the thickness of unconsolidated cover varies from about 1.2 m at the west end of the 55-m profile to zero at the east end. The difference in the interpretive sections between shooting west from the east end of spread 1 and shooting east from the west end of spread 2 suggests that the refractors are dipping down to the east beneath the shot point. The velocity of the interpreted bedrock layer is significantly higher at the west end of L2, and the travel-time curve offsets suggest faulting.

The travel-time curves of refraction line L1 (figs. 19-22) strongly suggest normal faulting of the bedrock. Accordingly, the computer-generated depth solution (see fig. 25a) for profile

L1 has been interpreted using faulting to accomplish changes in depth to the refractors. In this solution, an average upper layer velocity of 600 m sec^{-1} was used, and from the discussion of profiles L3 and L4, this layer includes both the unconsolidated material and the weathered bedrock. Because the time delay of the surface layer is only approximated by this technique, the upper layer depths in this model represent maximum depths for this layer. Derivation of the fault block model of figure 25b utilized the residual gravity profile along the line from plate 32B, as well as the results from the refraction data. The gravity profile is shown on figure 25a; with few exceptions the gravity gradients agree well with the offsets in the layers of the refraction solution. Layer 2 thins abruptly to the west of 413S, 185E, and the increase in residual gravity west of this point along the profile suggests that layer 3 has a higher density. The number of inferred faults and the spacing between them along the profile agrees well with that of the faults and fractures in the zones of quartz veining to the west (see pl. 1).

In figure 27, profiles from the residual gravity map (pl. 32B) have been plotted along trenches 3 and 4 of Bagdady and others (1978, pl. 1) with the corresponding depth of unconsolidated material, also from Bagdady and others (1978), plotted below each gravity profile. For unit density contrast, a gravity effect of about 0.04 mgal would be expected for each meter of change in thickness of the alluvium. Examination of the profiles reveals no systematic relationship between gravity anomalies and the alluvium, which is of an essentially constant thickness of about 2 m. The gravity anomalies amount to a few tenths of mgals, and thus are much too large to be explained by any reasonable variations in bulk density of so thin a layer of unconsolidated material. The anomalies are therefore attributed to lateral changes in bulk density of the underlying bedrock, probably resulting principally from extensive faulting.

Because of the shallow depth of cover, the large variations in seismic velocity and bulk density, the intensity of faulting and fracturing, and the very shallow nature of the alluvial channels, neither seismic refraction nor gravity surveying are adequate to delineate uniquely the channel pattern covered by the unconsolidated material. Therefore, additional placer deposit exploration would require other methods. On the other hand, both shallow seismic refraction and detailed gravity surveys appear to work quite well in distinguishing the near-surface bedrock structure.

Inferred fault and fracture pattern

A qualitative interpretation of the residual-gravity map (pl. 32B) and the magnetic-field map (pl. 27) in the area of the gravity survey was completed with the objective of extending the structural interpretation of figure 25b into a three-dimensional model. The procedure consisted of identifying (by inspection)

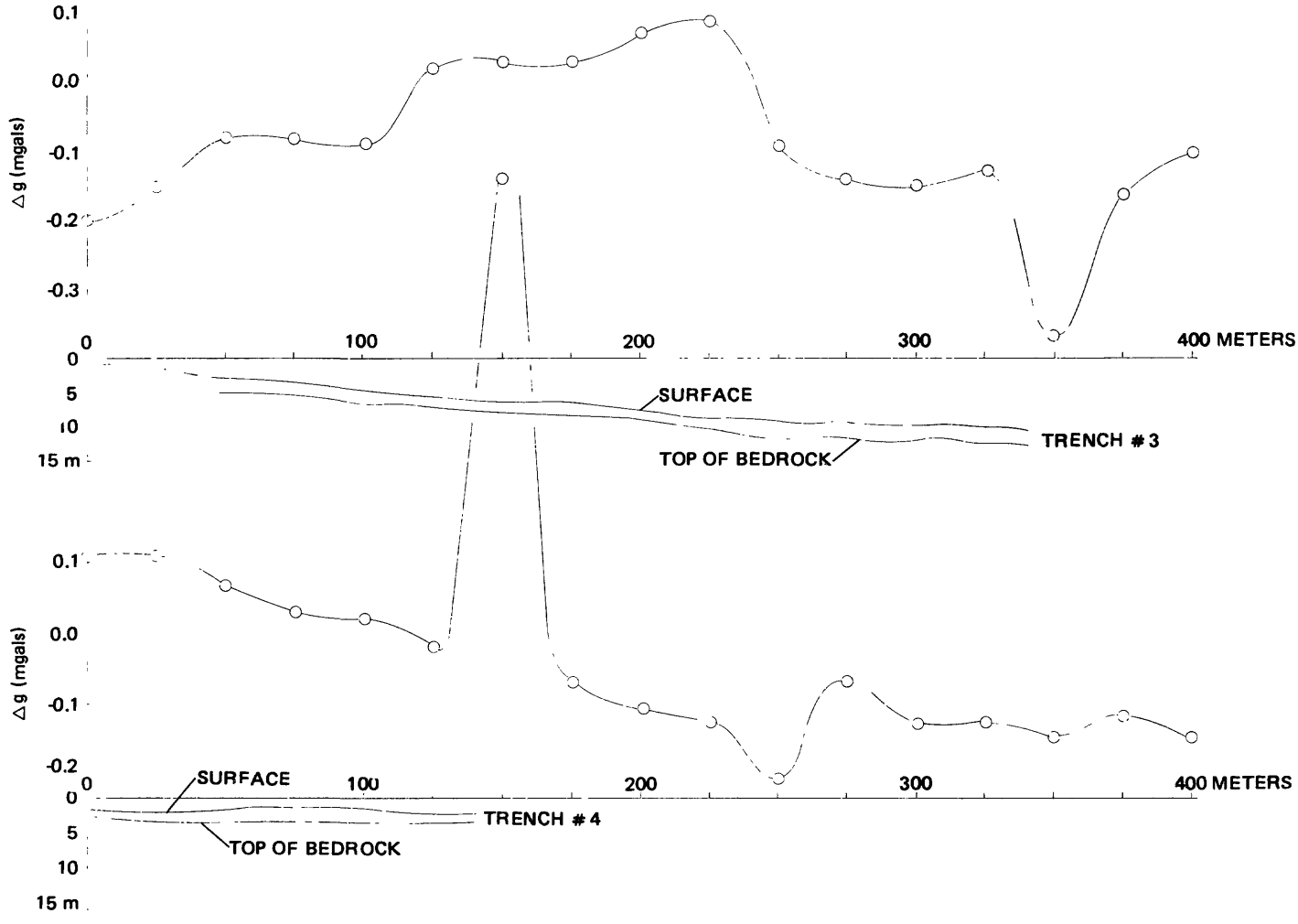

Figure 27.–Comparisons of residual Bouguer gravity anomaly with thickness of alluvial cover determined from trenching by Bagdady, and others (1978). Variations in thickness and density of the alluvium seem adequate to explain only about 0.05 mgal variations in the residual gravity; see text for a detailed explanation.

and drawing the steepest parts of gradients of both the gravity and magnetic anomalies onto a map sheet. From the resulting gradient map, bulk density and(or) magnetization contrast boundaries were inferred. For the magnetic anomaly gradients, normal polarization was assumed, so that at this magnetic latitude for a north-south profile (see fig. 16) the gradient falls over the body, and the anomaly maximum and minimum are roughly over the edges of the causative body. For an east-west profile, the steepest gradients are approximately over the edges of the body. The boundaries so defined identify blocks of contrasting magnetization and bulk density, and these boundaries are inferred to map a minimum distribution of faults and fractures, although it is recognized that some may be stratigraphic units of differing physical properties. However, the paucity of mapped strikes of beds in north to northeasterly directions on plate 1 suggests that the inferred structures are mostly faults and fractures. The gravity and magnetic gradients and the fault and fracture pattern inferred from them are displayed on plate 33.

The fault and fracture pattern (hereafter referred to as the fault pattern) of plate 33 shows several interesting features. The main trends are 030°-060°, 130°-150°, and 350°-010°. Two zones of northwest-trending penetrative structures that truncate or offset the pattern are obvious; one zone crosses the map from 280S, 100E to 500S, 500E and is quite sharply defined. The other is a broader zone and crosses the map from 075S, 100E to 250S, 500E. South of the southern penetrative structure, both northeast- and north-trending faults occur, whereas north of this structure the north-trending faults predominate. Both of the penetrative structures are aligned with mapped fault zones on plate 1.

The overall pattern suggests two alternative hypotheses. One is that this pattern is the result of a north- to northeast-trending set of faults that has been offset by a left-lateral strike-slip fault system trending northwest. Drag and rotation of blocks within the system rotated original northwest-trending faults to north-trending faults. The second hypothesis is that the northeast-trending faults are tensional fractures developed from folding on an axis plunging northeast and that the curvilinear fractures, whose surface traces curve around from northeastern to northern and northwestern trends, represent bedding plane slip. This set of faults, resulting from the folding, has subsequently been subjected to northwest-trending left-lateral strike-slip faulting of lesser intensity. In light of the geologic evidence (Goldsmith and Kouther, 1971; Luce and others, 1976; and Worl, 1978b), the latter hypothesis is the most likely; the northwest-trending strike-slip faulting probably occurred later and is related to the Najd fault system.

The density of faults on plate 33 is somewhat less than in the areas of exposed bedrock (pl. 1). Presumably this is because

not all the faults and fractures bring units of contrasting physical properties into juxtaposition, and thus they are not detectable by measurement of the gravity and magnetic fields.

Correlation map

Comparison of the various maps discussed and delineation of target zones are facilitated by a "correlation" map (pl. 34) on which the plan outlines of all significant geophysical anomalies have been traced.

The correlation map clearly outlines several areas of anomalous response to multiple geophysical methods that may be considered exploration targets. Also, spatial relationships between anomalous responses from different surveys can be identified. When this map is used, the areal distribution of the various surveys (that is, the surveys do not all cover the same area; see fig. 2), must be borne in mind in order to avoid erroneous conclusions.

The major relations are as follows: The TURAM anomalies are also areas of low apparent resistivity in areas where data for both are available. This relationship is expected if these areas are interpreted as electrically conductive fault zones. Low apparent-resistivity anomalies only occur in areas of anomalous induced polarization (IP) response in about half the cases, and then they are not usually coincident.

Furthermore, the low apparent-resistivity areas do not coincide with the areally large and intense IP anomalies, except where a TURAM anomaly is also present. Self-potential (SP) anomalies generally occur on the flanks of the IP anomalies, especially to the north or south. Areas of anomalous potassium-40 concentration do not in general correlate with any patterns shown by the other methods except in the areas of the mine workings along the north side of Jabal Mahd adh Dhahab. A few false correlations occur where alluvial material from bedrock areas of potassium alteration has been deposited in wadi courses over areas of anomalous response to other methods. Since gamma-radiation surveys penetrate only approximately 1 m, no correlation with the areas of high IP response beneath the pediment is expected.

When the inferred fault pattern of plate 33 is superimposed on plate 34, a reasonably good correlation is observed, particularly in the southern half of plate 33. The observed relationships are consistent with a model in which the mineralization follows the north-and northeast- trending faults and fractures and spreads out laterally from them downdip to the north along favorable horizons. The SP anomalies generally occur at the southern end of these systems, reflecting the shallower depth of penetration of the method, whereas the IP anomalies, with a greater penetration, extend north from the SP anomalies. The curvilinear faults in the western half of plate 33, which

strongly suggest folding, contain the major IP and most of the SP anomalies. The eastern edge of the fault system appears to constitute an eastern boundary for the mineralization. With the exception of one IP anomaly and part of the most extensive SP anomaly, the northwest-trending penetrative structures discussed above do not seem to have anomalies that suggest mineralization along them. In addition, northwest trends are generally lacking in the IP anomalies, and for these reasons the northwest structures are interpreted to be postmineralization, in agreement with geologic evidence (Worl, 1978b).

Comparison to bedrock geology

In areas of exposed bedrock, the geophysical maps and the correlation map may be compared directly with the mapped geology of plate 1. Some of the observations resulting from this comparison are discussed below.

The areas of anomalous concentrations of potassium-40 (ignoring those associated with wadi deposits) generally correlate with zones of intensive quartz veining, but the converse is not true. The outlines of the anomalous areas are generally controlled in the northwest-southeast direction by faults or lithologic contacts, and the most extensive areas of high potassium concentration occur in the tuffs, including the belt along the workings on the north side of Jabal Mahd adh Dhahab.

The large magnetic anomalies appear to be universally due to fault blocks of andesitic lavas.

The open-pit workings in the area of 350N, 000E correspond to a relatively strong SP anomalous response; the west end of the larger SP anomaly in the southern target area where it is on bedrock (approximately 400S, 050E) correlates with a zone of intrusive quartz veining and known sulfide mineralization. Finally, those SP anomalies occurring on bedrock are usually associated with zones of quartz veining and(or) outcrops mapped as agglomerates.

Although relatively few IP anomalies occur on bedrock and many are of the single-point variety, they do tend to cluster and occur in the agglomerates. Further, the clusters in the southern area tend to follow crudely the tuff-agglomerate contact. In the area of 450S, 050W sulfide mineralization is present, and the large IP anomaly to the east is a logical extension along strike.

The areas of low apparent resistivity occur mainly in zones of quartz veining, but the converse statement is not true. The apparent-resistivity anomalies occur particularly where zones of quartz veining are intersected by northwest-trending fault zones, and many of the resistivity anomalies have northwest orientations.

The only TURAM electromagnetic anomaly occurring on bedrock is located on the open pit (350N, 050E) and, so far as it can be defined from the data coverage, indicates a narrow, steeply dipping conductive zone striking northeast.

No meaningful correlation of the lithologies with the residual gravity field can be attempted because of insufficient data coverage on exposed bedrock.

Comparison of the correlation map of plate 34 with the gold and copper geochemical anomalies shown on plate 2 yields some correlation in the area of the mine workings with the SP, TURAM, and IP anomalies and some correlations elsewhere, particularly with the copper anomalies. However, especially in the south, the relationships are not systematic, and some geochemical anomalies have no geophysical signature. The probable explanation is that, although the anomalous elemental concentrations are preserved in the weathered outcrops from which the geochemical samples were taken, the sulfides themselves have been altered down to a substantial depth below the surface to mineral phases that do not respond to the IP or SP methods. Given the general northward dip of rocks of the area, the geophysical anomaly corresponding to a geochemical one would be expected to be displaced northward; in some cases this is true. In other cases, however, no geophysical anomaly is obvious, perhaps because it is so weak that it is not presently recognized. In addition, the gold and copper geochemical anomalies need not all be associated with sulfide mineralization. Many of the geochemical anomalies are controlled by fracture zones and lithologic variations, especially carbonate zones (Worl, oral commun., 1979), and these would not be expected to have a geophysical response.

Exploration targets

The major exploration targets outlined by this study are shown on the correlation map (pl. 34) as blocks of polygonal outline with a numerical label. Three areas are considered to be of first-order importance and are labeled 1.1, 1.2, and 1.3, and two considered to be of second-order importance are labeled 2.1 and 2.2. The areas of first-order importance are worthy of further exploration to test the significance of the geophysical anomalies defining them. Area 1.1 is the area of maximum IP response and essentially on-strike with areas of exposed sulfide mineralization. Area 1.2 has been partially tested by drill hole MD 10 (Worl, 1978b), drilled on the TURAM anomaly, but the IP anomalies on the eastern side of the major fault zone have not been adequately tested. A comparison of the correlation map with the geology of the 300-ft level from the SAMS mining activities (see Worl, 1978b), under the assumption that this fault zone is the northeast-trending, right-lateral fault system of Goldsmith and Kouther (1971, pl. 1), suggests that the northern part of the IP anomalies on the eastern side is associated with an offset of SAMS number 1 vein system. The offset would be of the order of

50 m or more. Detailed geophysical surveying on this area, including the tailings pond area, might better define the target.

Although the IP anomaly that defines area 1.3 occurs only for one electrode configuration, its proximity to the known mineralized zone intersected by hole MD 8 (Worl, 1978b) justifies its consideration as a first-order target. This area meets all the conditions of the model of mineralization and is also a promising area for geological reasons.

The two second-order targets need further definition. Extending the geophysical surveys northward would improve anomaly definition on both of these areas because they occur at the edge of the map area. Neither area has been tested by drilling. The persistence of anomalous responses in both areas and the position of both areas downdip from the tuff-agglomerate contact and zones of intensive quartz veining and mineralization suggests that they constitute exploration targets. Both zones are rated second order here because they lack the overall intensity of response of the other areas. However, both are likely to be more deeply buried, thus accounting for the weaker responses, and when adequate surveys are available to define them, they may become first-order exploration targets.

None of the geophysical results, including the aeromagnetic surveys, have yet given any indication of the source of the quartz veins that were responsible for the mineralization. R. G. Worl (oral commun., 1978) has suggested that the veins are part of a low-temperature hydrothermal system, which might not have required a magmatic event. The negative evidence from the geophysical work to date supports this hypothesis. All the geophysical results appear to be consistent with the following model, in which most of the structural elements are related to folding about an axis plunging to the northeast. The north- and northeast-trending fractures and faults seem to be mostly tensional in nature, and the low-angle faults mapped so far are more or less concentric to the fold axis; therefore both may be the result of the folding event. The quartz veining may perhaps have come from mobilized silicic material in the core of the fold, thus filling existing fractures as observed and providing the vehicle for metallization. Subsequently, faulting along northwest trends, probably part of the Najd fault system, has broken and offset units in a left-lateral sense.

CONCLUSIONS AND RECOMMENDATIONS

Geophysical investigations in the Mahd adh Dhahab district utilizing induced polarization (mise a la masse), self-potential, apparent resistivity, TURAM, and gamma radiation ground surveys of the magnetic and gravity fields, several shallow seismic refraction profiles, electric well logs, and laboratory studies of electrical and magnetic properties of the rocks of the district have yielded substantial insights into the geology of the district. Interpretation of the data resulted in a reasonable geologic picture of the bedrock beneath the alluvial cover immediately surrounding Jabal Mahd adh Dhahab and has delineated five target areas suitable for further exploration.

The combined geophysical and geological results favor a genetic model in which the principal structural elements are a northeast-plunging antiform and associated quartz veins, some of which carried mineralizing fluids, which fill tensional fractures apparently derived from the folding. The Mahd adh Dhahab district occurs on the nose of this antiform. Mineralization occurs in favorable agglomeratic horizons where they are capped by tuffs and intersected by zones of intense quartz veining. The geophysical surveys have delineated the eastern and northern boundaries of the antiform, but the western boundary has yet to be defined in detail, although geologic evidence suggests that the western edge of the mineralization may be the western edge of the zone of intense quartz veining (R. G. Worl, written commun., 1979). However, if the northwestern geophysical target (target 2.1, pl. 34) proves to be mineralized, a further westward extension may be possible. Both the geologic and geophysical data imply that the quartz veining is controlled by north- and northeast-trending tensional fractures and faults and to some extent by north-trending low-angle faults. Both types of faulting are probably related to the folding that created the antiform, and perhaps the folding and associated shearing are responsible for the mobilization of quartz for the veining. Mineralization accompanying the quartz veining is either syn- or postfolding, and finally there is both geologic and geophysical evidence for district-wide northwest-trending faults with a left-lateral strike-slip component. Postmineralization northeast-trending strike-slip faults may also be present. There is no substantial geophysical evidence for mineralization along the northwest-trending penetrative structures.

The results of the electric well-logging and paleomagnetic studies strongly suggest that the middle part of the stratigraphic succession probably consists of only two units, a lower agglomeratic unit overlain by a tuffaceous one, which have been structurally repeated at least once in the district.

Laboratory analysis of the magnetic properties of the rocks of the district, combined with geologic evidence from surface and subsurface mapping and the drill holes, indicates that the major

magnetic anomalies that occur in the covered areas are probably due to fault blocks of andesitic lavas, although intrusive bodies as a source of the anomaly are not totally ruled out.

Laboratory measurements of electrical properties of the rocks of the district indicate that, in general, induced polarization response increases with apparent resistivity. Because the rocks of the volcaniclastic pile are silicic and because, in addition, the sulfide mineralization is associated with zones of intense quartz veining, this relationship is not surprising.

Five target areas (pl. 34) are believed to justify further detailed surveys and exploratory drilling.

Of the geophysical investigations carried out in the Mahd adh Dhahab district, no one method produced either unique or unambiguous results. In general, the anomalous responses from most of the surveys were rather small and difficult to interpret. A synthesis of all the geological and geophysical data, however, yielded substantial insight into the geologic structure of the area, in addition to defining exploration targets. This study is a good example of the utility of a synergistic approach to exploration and suggests that a close corroboration between geologic and multimethod geophysical investigations might be profitably applied to other areas.

REFERENCES CITED

Andreasen, G. E., and Zietz, Isidore, 1969, Magnetic fields for a 4 x 6 prismatic model: U. S. Geological Survey Professional Paper 666, 9 p.

Arabian Geophysical and Surveying Company, 1975, Geophysical Surveys in North Samran district and Mahd adh Dhahab area: Arabian Geophysical and Surveying Company (ARGAS) Report 75-ARG-08, 47 p.

Bagdady, A. Y., Whitlow, J. W., and Roberts, R. J., 1978, Placer gold deposits in the Mahd adh Dhahab district, Kingdom of Saudi Arabia: U.S. Geological Survey Open-File Report 78-1074, ((IR) SA-235), 41 p.

Bevington, P. R., 1969, Data reduction and error analysis for the physical sciences: New York, McGraw-Hill, 336 p.

Blank, H. R., Flanigan, V. J., Gettings, M. E., and Merghelani, H. M., 1980, Geophysical investigations of the Kutam ancient mine and vicinity, Kingdom of Saudi Arabia: U. S. Geological Survey Open-File Report 80-1268 ((IR)SA-278), 53 p., 8 pls.

Davis, W. E., Allen, R. V., and Akhrass, M. N., 1972, Geophysical exploration in the Mahd adh Dhahab district, Saudi Arabia: U. S. Geological Survey Open-File Report (IR)SA-14, 4 p.

Geometrics, 1978, Radioelement assay with portable gamma spectrometers: Sunnyvale, California, Geometrics Technical Report Number 17, 5 p.

Godson, R. H., 1974, GEOPAC: U. S. Geological Survey Open-File Report (IR)SA-162, 146 p.

Goldsmith, Richard, and Kouther, J. H., 1971, Geology of the Mahd adh Dhahab-Umm ad Damar area, Kingdom of Saudi Arabia: Saudi Arabian Directorate General of Mineral Resources Bulletin 6, 20 p.

Grant, F. S. and West, G. F., 1965, Interpretation theory in applied geophysics: New York, McGraw-Hill, 583 p.

Heiland, C. A., 1940, Geophysical exploration: New York, Prentice-Hall, 1013 p.

Hunting Surveys Ltd., 1962, Airborne magnetometer-scintillation counter survey, Aqiq area: Saudi Arabian Directorate General of Mineral Resources unpublished maps, sheets 3 and 5, scale 1:50,000. (Information on these maps may be obtained by writing Deputy Minister of General Resources, P. O. Box 345, Jiddah, Saudi Arabia)

Ketola, Matti, 1972, Some points of view concerning mise a la masse measurements: Geoexploration, v. 10, p. 1-21.

Luce, R. W., Bagdady, A. Y., and Roberts, R. J., 1976, Geology and ore deposits of the Mahd adh Dhahab district, Kingdom of Saudi Arabia: U.S. Geological Survey open-file Report 76-865 ((IR)SA-195), 28 p., 1 pl.

Roberts, R. J., Bagdady, A. Y., and Luce, R. W., 1978, Geochemical investigations in the Mahd adh Dhahab district, Kingdom of Saudi Arabia, with a section on Computer analysis by L. D. North and I. H. Abuttahir: U.S. Geological Survey Open-File Report 78-777, ((IR)SA-231), 55 p., 1 pl.

Sumner, J. S., 1976, Principles of induced polarization for geophysical exploration: Amsterdam, Elsevier, 277 p.

Telford, W. M., Geldart, L. P. Sheriff, R. E., and Keys, D. A., 1975, Applied geophysics: New York, London, Cambridge University Press, 877 p.

Worl, R. G., 1978a, Ore controls at the Mahd adh Dhahab gold mine, Kingdom of Saudi Arabia: U.S. Geological Survey Open-File Report 78-778, ((IR)SA-232), 31 p., 1 pl.

Worl, R. G., 1978b, Mineral exploration-Mahd adh Dhahab district, Kingdom of Saudi Arabia: U.S. Geological Survey Open-File Report 78-1073, ((IR)SA-233), 89 p., 3 pls.